NASA Technical Memorandum 100097

High-Resolution Shock-Capturing Schemes for Inviscid and Viscous Hypersonic Flows

H. C. Yee, Ames Research Center, Moffett Field, California
G. H. Klopfer, NEAR Inc., Mountain View, California
J.-L. Montagné, ONERA, B. P. 72, 92322 Chatillon Cedex, France

April 1988

National Aeronautics and
Space Administration

Ames Research Center
Moffett Field, California 94035

HIGH-RESOLUTION SHOCK-CAPTURING SCHEMES FOR INVISCID AND VISCOUS HYPERSONIC FLOWS[1]

H.C. Yee[2]
NASA Ames Research Center, Moffett Field, CA 94035 USA
G.H. Klopfer[3]
NEAR Inc., Mountain View, CA 94043 USA
and
J.-L. Montagné[4]
ONERA, B.P. 72, 92322 Chatillon Cedex, France

Abstract

A class of implicit Total Variation Diminishing (TVD) type algorithms suitable for transonic and supersonic multidimensional Euler and Navier-Stokes equations has been extended to hypersonic computations. The improved conservative shock-capturing schemes are spatially second- and third-order, and are fully implicit. They can be first- or second-order accurate in time and are suitable for either steady or unsteady calculations. Enhancement of stability and convergence rate for hypersonic flows is discussed. With the proper choice of the temporal discretization and suitable implicit linearization, these schemes are fairly efficient and accurate for very complex two-dimensional hypersonic inviscid and viscous shock interactions. This study is complimented by a variety of steady and unsteady viscous and inviscid hypersonic blunt-body flow computations. Due to the inherent stiffness of viscous flow problems, numerical experiments indicated that the convergence rate is in general slower for viscous flows than for inviscid steady flows.

I. Motivation and Objective

Most shock-capturing methods are either inefficient for practical computations or only valid for transonic or supersonic perfect gas calculations. For hypersonic, perfect gas, equilibrium real gases or nonequilibrium flows, improvement and modification to existing methods are necessary. In addition, viscous hypersonic and nonequilibrium flow problems are generally stiff and implicit methods are generally preferred over explicit methods. Some of the numerical issues for steady inviscid hypersonic blunt-body flow computations were addressed in our earlier paper [1]. A semi-implicit method and a fully implicit method for steady-state nonequilibrium flows were discussed in Yee and Shinn [2]. A basic study on numerical methods for unsteady inviscid nonequilibrium flows was presented in LeVeque and Yee [3]. The objective of this research is to efficiently extend and improve as well as to present an unified formulation of the existing implicit high-resolution shock-capturing schemes [4-6,2] for multidimensional compressible Euler and Navier-Stokes equations in the hypersonic, perfect and equilibrium real gas flow regimes.

---

[1]An abbreviated version will appear in the proceedings of the BAIL V Conference, June 20-24, 1988, Shanghai, China.
[2]Research Scientist, Computational Fluid Dynamics Branch
[3]Research Scientist
[4]Research Scientist, Theoretical Aerodynamics Division, this work was performed while on leave as an Ames Associate at NASA Ames Research Center, Moffett Field, CA 94035 USA.

The improved schemes are based on a class of implicit Total Variation Diminishing (TVD) type algorithms originally designed for transonic and supersonic multidimensional Euler and Navier-Stokes equations [4-6]. The extended conservative shock-capturing schemes are spatially second- and third-order, and are and fully implicit. They can be first- or second-order accurate in time and are suitable for either steady or unsteady calculations. In addition, the current unified formulation allows the inclusion of the MUSCL-type approach [7] in conjunction with a local characteristic approach [24,6] or flux-vector splittings [8] (see section II for an explanation). For the present study, particular emphasis is placed on second-order implicit time-accurate high-resolution algorithms. The algorithms are formulated in finite volume and pseudo finite volume forms which, for certain physical problems and grid distributions, can enhance stability and convergence rate for highly clustered or skewed grids and require only a slight modification from the form originally presented in Yee and Harten [5] for generalized geometries. It is emphasized here that the use of the term TVD-type schemes pertains to the property of the algorithm as applied to one-dimensional nonlinear scalar hyperbolic conservation laws or constant coefficient hyperbolic systems in a semidiscrete sense. Theoretical justification of the proposed fully discretized schemes on the preservation of TVD property for the general nonlinear scalar hyperbolic conservation laws is under investigation. Moreover, the high-resolution property of these schemes for multidimensional nonlinear systems of hyperbolic conservation laws is evaluated by numerical experiments. In particular the following numerical issues are addressed:

1. Some numerical aspects of TVD-type schemes that affect the convergence rate for hypersonic Mach numbers and real gas flows but have negligible effect on low Mach number or perfect gas flows are identified.

2. The performance of the various linearized implicit forms of the proposed schemes similar to the transonic flow study [4-6] is reexamined for hypersonic flows.

3. The behavior of the proposed schemes with various temporal differencing but similar spatial discretization for inviscid and viscous flows is investigated. Studies indicated that their behavior in terms of stability and convergence rate is quite different between viscous and inviscid flows. However, with the proper choice of the temporal discretization and suitable implicit linearization, these schemes are fairly efficient and accurate for very complex two-dimensional hypersonic inviscid and viscous shock interactions.

4. The relative efficiency and accuracy of typical TVD-type schemes [9-11] for shock wave computations are examined. A comparative study on steady and unsteady flows reveals that the proposed class of TVD-type schemes, in particular, for equilibrium real gas and nonequilibrium flows, produces just as accurate shock resolution and yet requires less operations count than most other TVD schemes (e.g., higher-order Godunov [10], Osher & Chakravarthy [9], and TVD flux-vector splitting approaches [8]).

In the following section, the generalization of Roe's approximate Riemann solver and flux-vector splitting for real gases are reviewed. A description of the two-parameter family implicit shock-capturing scheme, the various enhancements on numerical stability and convergence rate for hypersonic flows, and the behavior of the scheme for inviscid and viscous flows are discussed in the subsequent sections. To illustrate the performance of the schemes for complex hypersonic flows, some representative numerical examples are also discussed.

II. Description of the Numerical Algorithm

The conservation laws for the two-dimensional Navier-Stokes equations can be written in the form

$$\frac{\partial U}{\partial t} + \frac{\partial F}{\partial x} + \frac{\partial G}{\partial y} = \frac{1}{Re}\left[\frac{\partial F_v}{\partial x} + \frac{\partial G_v}{\partial y}\right], \tag{1a}$$

where $U = [\ \rho,\ m,\ n,\ e\ ]^T$, $F = [\ \rho u,\ mu+p,\ nu,\ eu+pu\ ]^T$, $G = [\ \rho v,\ mv,\ nv+p,\ ev+pv\ ]^T$, $F_v = [\ 0,\ \tau_{xx},\ \tau_{xy},\ f\ ]^T$, and $G_v = [\ 0,\ \tau_{xy},\ \tau_{yy},\ g\ ]^T$. Here ρ is the density, u and v are the velocity components, $m = \rho u$ and $n = \rho v$ are the x- and y-components of the momentum per unit volume, p is the pressure, $e = \rho[\epsilon + \frac{1}{2}(u^2+v^2)]$ is the total energy per unit volume, and ϵ is the specific internal energy. For a perfect gas, we also have

$$\tau_{xx} = \mu(4u_x - 2v_y)/3, \tag{1b}$$

$$\tau_{xy} = \mu(u_y + v_x), \tag{1c}$$

$$\tau_{yy} = \mu(-2u_x + 4v_y)/3, \tag{1d}$$

$$f = u\tau_{xx} + v\tau_{xy} + \mu Pr^{-1}(\gamma-1)^{-1}\frac{\partial a^2}{\partial x}, \tag{1e}$$

$$g = u\tau_{xy} + v\tau_{yy} + \mu Pr^{-1}(\gamma-1)^{-1}\frac{\partial a^2}{\partial y}, \tag{1f}$$

where for example, u_x is defined as $\partial u/\partial x$. The dynamic viscosity μ is given by Sutherland's formula. The Reynolds number is Re, the Prandtl number is Pr, the sound speed is a, and the ratio of specific heats is γ.

Under a generalized coordinate transformation, $\xi = \xi(x,y)$ and $\eta = \eta(x,y)$, equation (1) can be written in a form which maintains the strong conservation-law form as

$$\frac{\partial \hat{U}}{\partial t} + \frac{\partial \hat{F}}{\partial \xi} + \frac{\partial \hat{G}}{\partial \eta} = \frac{1}{Re}\left[\frac{\partial \hat{F}_v}{\partial \xi} + \frac{\partial \hat{G}_v}{\partial \eta}\right], \tag{2}$$

where $\hat{U} = U/J$, $\hat{F} = (\xi_x F + \xi_y G)/J$, $\hat{G} = (\eta_x F + \eta_y G)/J$, $\hat{F}_v = (\xi_x F_v + \xi_y G_v)/J$, $\hat{G}_v = (\eta_x F_v + \eta_y G_v)/J$, and $J = \xi_x\eta_y - \xi_y\eta_x$, the Jacobian transformation. Let $A = \partial F/\partial U$ and $B = \partial G/\partial U$. Then the Jacobians $\hat{A} = \partial \hat{F}/\partial \hat{U}$ and $\hat{B} = \partial \hat{G}/\partial \hat{U}$ can be written as

$$\hat{A} = (\xi_x A + \xi_y B) \tag{3a}$$

$$\hat{B} = (\eta_x A + \eta_y B). \tag{3b}$$

In this study the thin-layer Navier-Stokes approximation is assumed by dropping all the $\partial(\cdot)/\partial\xi$ derivatives in the viscous terms. Also, stability and convergence rate viscous results are for a perfect gas and laminar flows with adiabatic wall conditions.

2.1. Riemann Solvers

Here the usual approach of applying the one-dimensional scalar TVD schemes via the so called Riemann solvers for each direction in multidimensional nonlinear systems of hyperbolic conservation laws (see for example reference [5,12]) is used. This approach is best suited for orthogonal or nearly orthogonal grids. The eigenvalues and eigenvectors of the Jacobian matrices $\hat{A}$ and $\hat{B}$ are used in approximate Riemann solvers. Given two states whose difference is ΔU, Roe [13] obtained an average $\overline{A}$ in the ξ-direction, for example, satisfying $\Delta\hat{F} = \overline{A}\Delta U$ for a perfect gas. The generalization by Vinokur [14] for an arbitrary gas involves the pressure derivatives $\chi = \left(\partial p/\partial\rho\right)_{\tilde{\epsilon}}$ and $\kappa = \left(\partial p/\partial\tilde{\epsilon}\right)_{\rho}$, where $\tilde{\epsilon} = \rho\epsilon$. The relation $c^2 = \chi + \kappa h$ then gives the speed of sound, where $h = \epsilon + p/\rho$. Introducing $H = h + (u^2+v^2)/2$, Vinokur found the same expressions for $\overline{u}, \overline{v}$ and $\overline{H}$ as for the perfect gas, and that $\overline{\chi}$ and $\overline{\kappa}$ must satisfy

$$\overline{\chi}\Delta\rho + \overline{\kappa}\Delta\widetilde{\epsilon} = \Delta p. \tag{4}$$

Unique values of $\overline{\chi}$ and $\overline{\kappa}$ are obtained by projecting the proper averages of the values for the two states into this relation (see references [14,11,12,15] for the exact formulas).

Flux-vector splitting methods divide the flux $\widehat{F}$ into several parts, each of which has a Jacobian matrix whose eigenvalues are all of one sign. The approach by Steger and Warming [16] made use of the relation $F = AU$, valid for a perfect gas. Van Leer [17] constructed a different splitting in which the eigenvalues of the split-flux Jacobians are continuous and one of them vanishes, leading to sharper capture of transonic shocks. Vinokur and Montagné [18] showed that the expressions for both these splittings can be generalized to an arbitrary gas by using the variable $\gamma = \rho c^2/p$, and adding to the split energy flux a term equal to the product of the split mass flux and the quantity $\epsilon - c^2/\left[\gamma(\gamma-1)\right]$ (see references [18,11,12,15] for the exact formulas).

The current study on the shock resolution of the various schemes [1,4-6,9] for two-dimensional steady-state blunt-body inviscid computations indicates similar trends as the one dimensional study [11]. The main issue appears to be their relative efficiency. Due to extra evaluations per dimension in the curve fitting between the left and right states in a real gas for the van Leer formulation, additional computation is required for the van Leer type schemes than the Harten and Yee [4,5,19], and Yee [6] types of TVD schemes. Here van Leer type schemes refer to the use of the MUSCL approach [7] (see section 2.2 for an explanation) in conjunction with the Roe type approximate Riemann solver [13] or flux-vector splittings [8] (hereafter the latter methods are referred to as the TVD flux-vector splitting methods). Moreover, for steady-state applications, implicit methods are preferred over explicit methods because of the faster convergence rate. In addition, it is easier to obtain a noniterative linearized implicit operator for the Harten and Yee, and Yee type schemes than for the van Leer type schemes. Furthermore, unlike flux-vector splitting approaches, implicit methods employing the Roe type approximate Riemann solver (non-MUSCL or MUSCL) with first-order implicit operators do not require the Jacobian of the $F^{\pm}$ and $G^{\pm}$ fluxes. Here $F^{\pm}$ is the portion of the flux with positive/negative eigenvalues. In many instances, the Jacobians of these fluxes are relatively difficult or expensive to obtain, in particular for nonequilibrium flows. A similar difficulty applies to the MUSCL formulations via the Roe type approximate Riemann solver if a spatially second-order implicit operator is desired. For these reasons, the linearized implicit versions of Harten and Yee [4] and Yee [6] are preferred over the van Leer type schemes. Consequently, numerical studies on the extension of the former schemes to hypersonic flows are emphasized. Some of these points will become more apparent when an unified formulation of these implicit methods is presented in section 2.2. An unified formulation of the corresponding explicit schemes can be found in reference [12].

2.2 Description of the Implicit TVD schemes

In the application of TVD-type schemes for viscous flows, the physical problems considered here are assumed to be inviscid dominated in the sense that moderate or strong shock waves are present in the flow field such that high-resolution shock-capturing techniques are required. Thus the numerical procedures used here for the compressible Navier-Stokes calculations are a second-order central difference approximation for the diffusion terms and TVD-type schemes for the inviscid part of the Navier-Stokes equations. The question of whether the present numerical dissipation term (due to the TVD-type terms) has an adverse effect on the true viscosity terms in the boundary layer region is not known at this point. What we can conclude from the current study is that the portions of the solution slightly or far away from the boundary layer are quite accurately simulated.

The two-parameter family of explicit and implicit high-resolution schemes presented here is based

on a semi-discrete methodology and on the one-parameter family of TVD-type algorithms developed in references [19,4-6]. The idea is to use the same spatial discretization as references [19,4-6] for the spatial derivatives and to use the two-parameter family of linear multistep methods for the time derivatives. The original one-parameter family of TVD-type schemes is a subset of the two-parameter family of algorithms. Mathematical analysis similar to that in [19,4-6] for the current larger family of schemes is under investigation. For a particular chosen time differencing, these schemes are TVD for the one-dimensional constant coefficient hyperbolic equations. Also the MUSCL approach in conjunction with the Roe-type approximate Riemann solver [2] and TVD flux-vector splitting methods [8] falls nicely into the present frame work. In other words, the present formulation includes a larger class of spatial as well as temporal discretization than in references [19,4-6].

Also, the formulation is in finite volume and pseudo finite volume forms which can enhance stability and convergence rate for highly clustered or skewed grids and is a slight modification from the form originally presented in Yee and Harten [5] for generalized geometries. For fairly uniform or mildly clustered grids, the present finite volume and pseudo finite volume forms behave the same as in reference [5] for inviscid flows. This is in contrast to the study of Takakura et al. [20] which claimed that their modified form [20] is the correct finite difference formulation for generalized geometries. A comparison between Takakura et al. [20] and reference [5] on the same fairly uniform curvilinear grid for a blunt-body computation shows no noticeable difference in resolution.

Without loss of generality, the two-parameter family of implicit schemes for the Euler equations ($F_v = G_v = 0$) is presented here. For general Navier-Stokes equations, the appropriate three-point central differences of the viscous Jacobian terms should be added to the implicit operator and a central difference approximation for the diffusion terms should be added to the explicit operator.

Let Δt be the time step and let the grid spacing be denoted by $\Delta\xi$ and $\Delta\eta$ such that $\xi = j\Delta\xi$ and $\eta = k\Delta\eta$. Also let $\lambda^\xi = \frac{\Delta t}{\Delta\xi}$ and $\lambda^\eta = \frac{\Delta t}{\Delta\eta}$; then a two-parameter family of explicit and implicit TVD-type algorithms in generalized coordinates for two-dimensional systems (1) with $F_v = G_v = 0$ can be written as

$$\Delta\hat{U}^n_{j,k} + \frac{\lambda^\xi\theta}{1+\omega}\left[\tilde{F}^{n+1}_{j+\frac{1}{2},k} - \tilde{F}^{n+1}_{j-\frac{1}{2},k}\right] + \frac{\lambda^\eta\theta}{1+\omega}\left[\tilde{G}^{n+1}_{j,k+\frac{1}{2}} - \tilde{G}^{n+1}_{j,k-\frac{1}{2}}\right]$$

$$= -\frac{(1-\theta)\lambda^\xi}{1+\omega}\left[\tilde{F}^n_{j+\frac{1}{2},k} - \tilde{F}^n_{j-\frac{1}{2},k}\right] - \frac{(1-\theta)\lambda^\eta}{1+\omega}\left[\tilde{G}^n_{j,k+\frac{1}{2}} - \tilde{G}^n_{j,k-\frac{1}{2}}\right] + \frac{\omega}{1+\omega}\Delta\hat{U}^{n-1}_{j,k}. \qquad (5)$$

Here $\Delta\hat{U}^n_{j,k} = \hat{U}^{n+1}_{j,k} - \hat{U}^n_{j,k}$. The functions $\tilde{F}_{j+\frac{1}{2},k}$ and $\tilde{G}_{j,k+\frac{1}{2}}$ are the numerical fluxes in the ξ- and η-directions evaluated at $(j+\frac{1}{2},k)$ and $(j,k+\frac{1}{2})$, respectively. This two-parameter family of algorithms contains first- and second-order implicit as well as explicit schemes. The scheme is temporally second-order if $\theta = \omega + \frac{1}{2}$ and first-order otherwise. When $\theta \neq 0$, algorithm (5) is an implicit scheme. In this paper, only the temporally first-order backward Euler ($\theta = 1$, $\omega = 0$) and the temporally second-order three-point backward differentiation ($\theta = 1$, $\omega = 1/2$) time-differencing are investigated. Detailed formulation and numerical studies for algorithm (5) with $\omega = 0$ for transonic, supersonic and hypersonic flows can be found in references [4-6,12,1,11,21,22]. The current study shows that, for viscous steady and unsteady flows, the temporally second-order implicit algorithm ($\theta = 1$, $\omega = 1/2$) appears to be slightly more stable and efficient than the temporally first-order implicit algorithm ($\theta = 1$, $\omega = 0$).

The spatial accuracy of equation (5) depends on the form of the numerical flux functions. There exists many ways to achieve higher-order spatial accuracy and at the same time have TVD-type properties. Here two of the ways are discussed. The first is due to Harten [19], Roe [23], and Yee-Roe-Davis [6,24,25], and the second, sometimes referred to as the MUSCL approach, is due to

van Leer [7]. Following the same nomenclature as in references [11,12], hereafter, we refer to the first way as the non-MUSCL approach. Besides the different temporally implicit discretization, the combination of the two Riemann solvers discussed in section 2.1 and higher-order spatial differencing considered yields three different types of spatial differencing for the nonlinear system (1): namely, non-MUSCL and MUSCL approaches using an approximate Riemann solver, and a MUSCL approach using flux-vector splittings (TVD flux-vector splitting methods).

Non-MUSCL Approach Using an Approximate Riemann Solver: The numerical flux function $\widetilde{F}_{j+\frac{1}{2},k}$ for a non-MUSCL type approach, together with the local characteristic approach [4-6] (Roe type of approximate Riemann solver) in a finite volume formulation, can be expressed as

$$\widetilde{F}_{j+\frac{1}{2},k} = \frac{1}{2}\left[\left(\frac{\xi_x}{J}\right)_{j+\frac{1}{2}}(F_{j,k}+F_{j+1,k}) + \left(\frac{\xi_y}{J}\right)_{j+\frac{1}{2}}(G_{j,k}+G_{j+1,k}) + R_{j+\frac{1}{2}}\Phi_{j+\frac{1}{2}}\Big/J_{j+\frac{1}{2}}\right]. \quad (6a)$$

The corresponding pseudo finite volume formulation will be discussed in section 2.4. Here $R_{j+\frac{1}{2}}$ is the eigenvector matrix for $\partial\widehat{F}/\partial U$ evaluated at some symmetric average of $U_{j,k}$ and $U_{j+1,k}$ (for example, Roe average [13] for a perfect gas and generalized Roe average of Vinokur [14] for real gases). The values

$$\left(\frac{\xi_x}{J}\right)_{j+\frac{1}{2}} = \frac{1}{2}\left[\left(\frac{\xi_x}{J}\right)_{j,k} + \left(\frac{\xi_x}{J}\right)_{j+1,k}\right]; \qquad \frac{1}{J_{j+\frac{1}{2}}} = \frac{1}{2}\left(\frac{1}{J_{j+1,k}} + \frac{1}{J_{j,k}}\right). \quad (6b)$$

Also $(k_1)_{j+\frac{1}{2}} = \left[\frac{\xi_x}{J}\Big/\sqrt{\left(\frac{\xi_x}{J}\right)^2+\left(\frac{\xi_y}{J}\right)^2}\right]_{j+\frac{1}{2}}$ and $(k_2)_{j+\frac{1}{2}} = \left[\frac{\xi_y}{J}\Big/\sqrt{\left(\frac{\xi_x}{J}\right)^2+\left(\frac{\xi_y}{J}\right)^2}\right]_{j+\frac{1}{2}}$ used in $R_{j+\frac{1}{2}}$ are defined, for example, as

$$(k_1)_{j+\frac{1}{2}} = \frac{\left(\frac{\xi_x}{J}\right)_{j+\frac{1}{2}}}{\sqrt{\left(\frac{\xi_x}{J}\right)^2_{j+\frac{1}{2}} + \left(\frac{\xi_y}{J}\right)^2_{j+\frac{1}{2}}}} \quad (6c)$$

. The values ξ_x, ξ_y, η_x and η_y are evaluated by three-point central differences. Similarly, one can define the numerical flux $\widetilde{G}_{j,k+\frac{1}{2}}$ in this manner.

Here the form of $\Phi_{j+\frac{1}{2}}$ can be divided into two types: (a) a spatially second-order symmetric TVD-type scheme [6,24,25] in which the numerical dissipation terms are independent of the sign of the characteristic speeds and (b) a spatially second-order upwind TVD-type scheme [19,5] in which the numerical dissipation terms depend on the sign of the characteristic speeds.

The elements of the $\Phi_{j+\frac{1}{2}}$ in the ξ-direction denoted by $(\phi^l_{j+\frac{1}{2}})^S$ for a spatially second-order symmetric TVD-type scheme [6,12] are

$$(\phi^l_{j+\frac{1}{2}})^S = -\psi(a^l_{j+\frac{1}{2}})\left[\alpha^l_{j+\frac{1}{2}} - \widehat{Q}^l_{j+\frac{1}{2}}\right]. \quad (7a)$$

The value $a^l_{j+\frac{1}{2}}$ is the characteristic speed a^l for $\partial\widehat{F}/\partial U$ evaluated at the same symmetric average between $U_{j,k}$ and $U_{j+1,k}$. The function ψ is

$$\psi(z) = \begin{cases} |z| & |z| \geq \delta_1 \\ (z^2+\delta_1^2)/2\delta_1 & |z| < \delta_1 \end{cases}. \quad (7b)$$

Here $\psi(z)$ in equation (7b) is an entropy correction to $|z|$ where δ_1 is a small positive parameter. For problems containing simple unsteady shocks, δ_1 is set to zero in most of the computations

since entropy-violating phenomena occur only for steady or nearly steady shocks. For steady-state problems containing strong shock waves, a proper control of the size of δ_1 is very important, especially for hypersonic blunt-body flows. The choice of δ_1 is also highly dependent on the Mach number and geometry of the physical problem. For the current numerical examples, the parameter δ_1 is set to be a function of a^l_ξ and a^l_η. See reference [12] or section III for a discussion.

Examples of the 'limiter' function $\widehat{Q}^l_{j+\frac{1}{2}}$ can be expressed as

$$\widehat{Q}^l_{j+\frac{1}{2}} = \text{minmod}(\alpha^l_{j-\frac{1}{2}}, \alpha^l_{j+\frac{1}{2}}) + \text{minmod}(\alpha^l_{j+\frac{1}{2}}, \alpha^l_{j+\frac{3}{2}}) - \alpha^l_{j+\frac{1}{2}} \tag{7c}$$

$$\widehat{Q}^l_{j+\frac{1}{2}} = \text{minmod}(\alpha^l_{j-\frac{1}{2}}, \alpha^l_{j+\frac{1}{2}}, \alpha^l_{j+\frac{3}{2}}) \tag{7d}$$

$$\widehat{Q}^l_{j+\frac{1}{2}} = \text{minmod}\left[2\alpha^l_{j-\frac{1}{2}}, 2\alpha^l_{j+\frac{1}{2}}, 2\alpha^l_{j+\frac{3}{2}}, \frac{1}{2}(\alpha^l_{j-\frac{1}{2}} + \alpha^l_{j+\frac{3}{2}})\right]. \tag{7e}$$

The minmod function of a list of arguments is equal to the smallest number in absolute value if the list of arguments is of the same sign, or is equal to zero if any arguments are of opposite sign. Here $\alpha^l_{j+\frac{1}{2}}$ are elements of

$$\alpha_{j+\frac{1}{2}} = R^{-1}_{j+\frac{1}{2}}(U_{j+1,k} - U_{j,k}). \tag{8}$$

The elements of the $\Phi_{j+\frac{1}{2}}$ in the ξ-direction denoted by $(\phi^l_{j+\frac{1}{2}})^U$ for a spatially second-order upwind TVD-type scheme [19,5,12] are

$$(\phi^l_{j+\frac{1}{2}})^U = \frac{1}{2}\psi(a^l_{j+\frac{1}{2}})(g^l_{j+1} + g^l_j) - \psi(a^l_{j+\frac{1}{2}} + \gamma^l_{j+\frac{1}{2}})\alpha^l_{j+\frac{1}{2}} \tag{9a}$$

where

$$\gamma^l_{j+\frac{1}{2}} = \frac{1}{2}\psi(a^l_{j+\frac{1}{2}})\begin{cases} (g^l_{j+1} - g^l_j)/\alpha^l_{j+\frac{1}{2}} & \alpha^l_{j+\frac{1}{2}} \neq 0 \\ 0 & \alpha^l_{j+\frac{1}{2}} = 0 \end{cases}. \tag{9b}$$

Examples of limiter function g^l_j used in calculations are

$$g^l_j = \text{minmod}(\alpha^l_{j-\frac{1}{2}}, \alpha^l_{j+\frac{1}{2}}) \tag{9c}$$

$$g^l_j = \left(\alpha^l_{j+\frac{1}{2}}\alpha^l_{j-\frac{1}{2}} + |\alpha^l_{j+\frac{1}{2}}\alpha^l_{j-\frac{1}{2}}|\right) \Big/ \left(\alpha^l_{j+\frac{1}{2}} + \alpha^l_{j-\frac{1}{2}}\right) \tag{9d}$$

$$g^l_j = \left\{\alpha^l_{j-\frac{1}{2}}\left[(\alpha^l_{j+\frac{1}{2}})^2 + \delta\right] + \alpha^l_{j+\frac{1}{2}}\left[(\alpha^l_{j-\frac{1}{2}})^2 + \delta\right]\right\} \Big/ \left[(\alpha^l_{j+\frac{1}{2}})^2 + (\alpha^l_{j-\frac{1}{2}})^2 + 2\delta\right] \tag{9e}$$

$$g^l_j = \text{minmod}\left(2\alpha^l_{j-\frac{1}{2}}, 2\alpha^l_{j+\frac{1}{2}}, \frac{1}{2}(\alpha^l_{j-\frac{1}{2}} + \alpha^l_{j-\frac{1}{2}})\right) \tag{9f}$$

$$g^l_j = S \cdot \max\left[0, \min(2|\alpha^l_{j+\frac{1}{2}}|, S \cdot \alpha^l_{j-\frac{1}{2}}), \min(|\alpha^l_{j+\frac{1}{2}}|, 2S \cdot \alpha^l_{j-\frac{1}{2}})\right];\ S = \text{sgn}(\alpha^l_{j+\frac{1}{2}}). \tag{9g}$$

Here δ is a small parameter. In practical calculations $10^{-7} \leq \delta \leq 10^{-5}$ is a commonly used range.

MUSCL Approach Using an Approximate Riemann Solver: The numerical flux function $\widetilde{F}_{j+\frac{1}{2},k}$ for a MUSCL type approach, together with Roe type of approximate Riemann solver, for an upwind scheme as described in Yee [26] and Yee & Shinn [2] can be expressed as

$$\tilde{F}_{j+\frac{1}{2},k} = \frac{1}{2}\left\{\left(\frac{\xi_x}{J}\right)_{j+\frac{1}{2}}\left[F(U^R_{j+\frac{1}{2}}) + F(U^L_{j+\frac{1}{2}})\right] + \left(\frac{\xi_y}{J}\right)_{j+\frac{1}{2}}\left[G(U^R_{j+\frac{1}{2}}) + G(U^L_{j+\frac{1}{2}})\right] + \widehat{R}_{j+\frac{1}{2}}\widehat{\Phi}_{j+\frac{1}{2}}\Big/ J_{j+\frac{1}{2}}\right\} \tag{10a}$$

The values $F(U^R_{j+\frac{1}{2}})$ and $F(U^L_{j+\frac{1}{2}})$ are the flux function F evaluated at $U^R_{j+\frac{1}{2}}$ and $U^L_{j+\frac{1}{2}}$ respectively, with

$$U^R_{j+\frac{1}{2}} = U_{j+1,k} - \frac{1}{4}\left[(1-\overline{\eta})\widetilde{\Delta_{j+\frac{3}{2}}} + (1+\overline{\eta})\widetilde{\widetilde{\Delta_{j+\frac{1}{2}}}}\right] \tag{10b}$$

$$U^L_{j+\frac{1}{2}} = U_{j,k} + \frac{1}{4}\left[(1-\overline{\eta})\widetilde{\widetilde{\Delta_{j-\frac{1}{2}}}} + (1+\overline{\eta})\widetilde{\Delta_{j+\frac{1}{2}}}\right] \tag{10c}$$

where $\overline{\eta}$ discussed below, is a parameter to control the spatial accuracy of the scheme. The limiters $\widetilde{\Delta_{j+\frac{1}{2}}}$ and $\widetilde{\widetilde{\Delta_{j+\frac{1}{2}}}}$ can be expressed as

$$\widetilde{\Delta_{j+\frac{1}{2}}} = \text{minmod}\left(\Delta_{j+\frac{1}{2}}, \beta\Delta_{j-\frac{1}{2}}\right) \tag{10d}$$

$$\widetilde{\widetilde{\Delta_{j+\frac{1}{2}}}} = \text{minmod}\left(\Delta_{j+\frac{1}{2}}, \beta\Delta_{j+\frac{3}{2}}\right) \tag{10e}$$

with

$$\text{minmod}(x, \beta y) = \text{sgn}(x)\cdot\max\left\{0, \min\left[|x|, \text{sgn}(x)\cdot\beta y\right]\right\} \tag{10f}$$

and $\beta = \frac{3-\overline{\eta}}{1-\overline{\eta}}$, where $\Delta_{j+\frac{1}{2}} = U_{j+1,k} - U_{j,k}$. For $\overline{\eta} = -1$, $\widetilde{\Delta_{j+\frac{1}{2}}}$ and $\widetilde{\widetilde{\Delta_{j+\frac{1}{2}}}}$ can be the same limiter as (9) except the arguments are now the $\Delta_{j\pm\frac{1}{2}}$ instead of $\alpha_{j\pm\frac{1}{2}}$.

The vector $\widehat{R}_{j+\frac{1}{2}}$ is the eigenvector of A evaluated at some symmetric average of $U^R_{j+\frac{1}{2}}$ and $U^L_{j+\frac{1}{2}}$; i.e.,

$$\widehat{R}_{j+\frac{1}{2}} = R_\xi(U^R_{j+\frac{1}{2}}, U^L_{j+\frac{1}{2}}) \tag{10g}$$

and the elements of $\widehat{\Phi}_{j+\frac{1}{2}}$ are

$$\widehat{\phi}^l_{j+\frac{1}{2}} = \psi(\widehat{a}^l_{j+\frac{1}{2}})\widehat{\alpha}^l_{j+\frac{1}{2}} \tag{10h}$$

where again $\widehat{a}^l_{j+\frac{1}{2}}$ and $\widehat{\alpha}^l_{j+\frac{1}{2}}$ are evaluated at some symmetric average of $U^R_{j+\frac{1}{2}}$ and $U^L_{j+\frac{1}{2}}$ and

$$\widehat{a}^l_{j+\frac{1}{2}} = a^l_\xi(U^R_{j+\frac{1}{2}}, U^L_{j+\frac{1}{2}}) \tag{10i}$$

$$\widehat{\alpha}_{j+\frac{1}{2}} = \widehat{R}^{-1}_{j+\frac{1}{2}}(U^R_{j+\frac{1}{2}} - U^L_{j+\frac{1}{2}}). \tag{10j}$$

Here the spatial order of accuracy pertaining to the scheme with the limiter not present (i.e., remove the tildes from equations (10b,c)) is determined by the value of $\overline{\eta}$. For example, if $\overline{\eta} = -1$ the scheme is fully upwind and if $\overline{\eta} = 0$ it is Fromm's scheme. When $\overline{\eta} = 1/3$ the scheme is third-order and when $\overline{\eta} = 1$ it is the regular three-point central difference scheme.

MUSCL Approach Using Flux-Vector Splittings: The numerical flux function $\tilde{F}_{j+\frac{1}{2},k}$ for a MUSCL-type approach, together with flux-vector splittings [8] referred as the TVD flux-vector splitting method in this paper can be expressed as

$$\tilde{F}_{j+\frac{1}{2},k} = \left(\frac{\xi_x}{J}\right)_{j+\frac{1}{2}} \left[F^-(U^R_{j+\frac{1}{2}}) + F^+(U^L_{j+\frac{1}{2}})\right] + \left(\frac{\xi_y}{J}\right)_{j+\frac{1}{2}} \left[G^-(U^R_{j+\frac{1}{2}}) + G^+(U^L_{j+\frac{1}{2}})\right] \tag{11}$$

where $F^{\pm}(U^{R,L}_{j+\frac{1}{2}})$ are evaluated using either the Steger-Warming type [16,18] or van Leer type [17,18] flux-vector splittings. The vectors $U^R_{j+\frac{1}{2}}$ and $U^L_{j+\frac{1}{2}}$ are the same as in equations (10b,c). The quantity $F^-(U^R_{j+\frac{1}{2}})$ is the portion of the flux F with negative eigenvalues evaluated at $U^R_{j+\frac{1}{2}}$.

The operations count between (6)-(9) and (10,11) is within 30% for a perfect gas. However, due to an extra evaluation per dimension in the curve fitting between the left and right states in an equilibrium real gas for (10,11), additional computation is required for the MUSCL approach. The slight advantage of (10,11) over (6)-(9) is that (10,11) can be spatially third-order accurate. However, experiences with the third-order case ($\bar{\eta} = 1/3$) do not show a very visible improvement over the second-order case for problems with discontinuities. Part of the reason is that all TVD-type schemes reduce to first-order at points of extrema regardless of the order of accuracy at smooth regions. Also, because of the similarity in shock resolution and yet higher operations count for real gases and nonequilibrium flows of the MUSCL over the non-MUSCL approach using Roe type approximate Riemann solver, efforts are concentrated only on the non-MUSCL formulation. At present no outstanding advantages or disadvantages between these formulations for a perfect gas have been observed. Further investigation is required along this line before a clearer comparison can be drawn.

2.3 A Conservative Linearized Implicit Form For Unsteady and Steady-State Calculations

To solve for U^{n+1} in (5) one normally needs to solve a set of nonlinear algebraic equations iteratively. One way to avoid this is to linearize the implicit operator and solve the linearized form by other means. Following the same procedure as in references [4-6], a conservative linearized alternating direction implicit (ADI) form of (5) for the numerical fluxes (6) and (10a) can be written as

$$\left[I + \frac{\lambda^\xi \theta}{1+\omega} H^\xi_{j+\frac{1}{2},k} - \frac{\lambda^\xi \theta}{1+\omega} H^\xi_{j-\frac{1}{2},k}\right]^n E^* = -\frac{\lambda^\xi}{1+\omega}\left[\tilde{F}^n_{j+\frac{1}{2},k} - \tilde{F}^n_{j-\frac{1}{2},k}\right] - \frac{\lambda^\eta}{1+\omega}\left[\tilde{G}^n_{j,k+\frac{1}{2}} - \tilde{G}^n_{j,k-\frac{1}{2}}\right] + \frac{\omega}{1+\omega}\Delta\hat{U}^{n-1}_{j,k}, \tag{12a}$$

$$\left[I + \frac{\lambda^\eta \theta}{1+\omega} H^\eta_{j,k+\frac{1}{2}} - \frac{\lambda^\eta \theta}{1+\omega} H^\eta_{j,k-\frac{1}{2}}\right]^n E^n = E^*, \tag{12b}$$

$$E^n = \Delta\hat{U}^n; \qquad \hat{U}^{n+1} = \hat{U}^n + E^n, \tag{12c}$$

where

$$H^\xi_{j+\frac{1}{2},k} = \frac{1}{2}\left[\hat{A}_{j+1,k} - \Omega^\xi_{j+\frac{1}{2},k}\right], \tag{12d}$$

$$H^\eta_{j,k+\frac{1}{2}} = \frac{1}{2}\left[\hat{B}_{j,k+1} - \Omega^\eta_{j,k+\frac{1}{2}}\right]. \tag{12e}$$

The nonstandard notation

$$H^\xi_{j+\frac{1}{2},k} E^* = \frac{1}{2}\left[\hat{A}_{j+1,k} E^*_{j+1,k} - \Omega^\xi_{j+\frac{1}{2},k} E^*\right] \tag{12f}$$

is used, and $\Omega^{\xi}_{j+\frac{1}{2},k}E^*$, $\Omega^{\eta}_{j,k+\frac{1}{2}}E$ can be taken as

$$\Omega^{\xi}_{j+\frac{1}{2},k}E^* = R_{j+\frac{1}{2},k}\mathrm{diag}\left[\psi(a^l_{j+\frac{1}{2}})\right]R^{-1}_{j+\frac{1}{2},k}(E^*_{j+1,k} - E^*_{j,k}) \tag{12g}$$

$$\Omega^{\eta}_{j,k+\frac{1}{2}}E = R_{j,k+\frac{1}{2}}\mathrm{diag}\left[\psi(a^l_{k+\frac{1}{2}})\right]R^{-1}_{j,k+\frac{1}{2}}(E_{j,k+1} - E_{j,k}). \tag{12h}$$

Here $\widehat{A}_{j+1,k}$, $\widehat{B}_{j,k+1}$ are Jacobians of $\widehat{F}$ and $\widehat{G}$ evaluated at $(j+1,k)$ and $(j,k+1)$. The value $E^n_{j,k} = \widehat{U}^{n+1}_{j,k} - \widehat{U}^n_{j,k}$. The expression $\mathrm{diag}(z^l)$ denotes a diagonal matrix with diagonal elements z^l.

The nonconserverative linearized implicit form suitable for steady-state calculations [4] is also considered. Numerical study indicated that the latter form appears to be slightly less efficient in terms of convergence rate than the linearized conservative form (12). This conservative linearized implicit operator as well as the nonconservative linearized implicit operator (both suggested in reference [4]) for $\theta = 1$, $\omega = 0$ was renamed two year later by Barth [27] as the approximate Jacobian linearization. To compute (12g,h), a triple matrix multiplication of dimension (4×4) has to be performed at every grid point. For steady-state applications, one can simplify (12g,h) as

$$\Omega^{\xi}_{j+\frac{1}{2},k}E = M_{\xi}I(E_{j+1,k} - E_{j,k}) \tag{13a}$$

$$\Omega^{\eta}_{j,k+\frac{1}{2}}E = M_{\eta}I(E_{j,k+1} - E_{j,k}) \tag{13b}$$

The scalar values M_{ξ} and M_{η} are

$$M_{\xi} = \max_l \psi(a^l_{j+\frac{1}{2}}) \tag{13c}$$

$$M_{\eta} = \max_l \psi(a^l_{k+\frac{1}{2}}) \tag{13d}$$

and I is the identity matrix. Note that (13a,b) involve scalar multiplication only. The solution using (13) is still second-order (or third-order) accurate after it reaches steady-state. Other linearized implicit forms can be found in references [4-6].

2.4 General Assumptions and Limitations on the Numerical Studies

The present study is by no means an exhaustive investigation. There are additional elements and parameters (other than the ones considered here) in the algorithm itself as well as in the physical problem, such as flow type and geometric complexity, that can affect or interfere with the performance of the numerical scheme. Even within the numerical issues listed in section I, the study is limited to a sampling of the parameter range for the time-step size or CFL number and the form of δ_1 in (7b). In particular, various strategies to speed up and stabilized the start-up solution from freestream conditions for steady computations have not been investigated. What is discussed here is intended to give interested readers some guideline for the use of the algorithm and to shed some light for further study and improvement of the scheme and the development of better ones. All of the numerical studies discussed in the subsequent sections rely on the following assumptions and considerations:

1. Although the recommended finite volume formulation (6) closely mimics the regular finite volume formulation for two dimensions, the results obtained in this report used a slightly different formulations than (6). In particular, three formulations (hereafter referred to as the pseudo finite volume formulations) for the non-MUSCL schemes were investigated and are as follows

$$\tilde{F}_{j+\frac{1}{2},k} = \frac{1}{2}\Big[(\xi_x)_{j+\frac{1}{2}}(F_{j,k} + F_{j+1,k}) + (\xi_y)_{j+\frac{1}{2}}(G_{j,k} + G_{j+1,k}) + R_{j+\frac{1}{2}}\Phi_{j+\frac{1}{2}}\Big] \Big/ J_{j+\frac{1}{2}} \tag{14a}$$

with the corresponding quantities $(\xi_x)_{j+\frac{1}{2}}$, $J_{j+\frac{1}{2}}$ and $(k_1)_{j+\frac{1}{2}}$ of equations (6b,c) express as

$$(\xi_x)_{j+\frac{1}{2}} = \frac{1}{2}\big[(\xi_x)_{j+1,k} + (\xi_x)_{j,k}\big]; \quad J_{j+\frac{1}{2}} = \frac{1}{2}\big[J_{j+1,k} + J_{j,k}\big], \tag{14b}$$

$$(k_1)_{j+\frac{1}{2}} = \frac{(\xi_x)_{j+\frac{1}{2}}}{\sqrt{(\xi_x)^2_{j+\frac{1}{2}} + (\xi_y)^2_{j+\frac{1}{2}}}}, \tag{14c}$$

and

$$\tilde{F}_{j+\frac{1}{2},k} = \frac{1}{2}\Big[(\xi_x F + \xi_y G)_{j,k} + (\xi_x F + \xi_y G)_{j+1,k} + R_{j+\frac{1}{2}}\Phi_{j+\frac{1}{2}}\Big] \Big/ J_{j+\frac{1}{2}} \tag{15}$$

and

$$\tilde{F}_{j+\frac{1}{2},k} = \frac{1}{2}\Big[\hat{F}_{j+1,k} + \hat{F}_{j,k} + R_{j+\frac{1}{2}}\Phi_{j+\frac{1}{2}} \Big/ J_{j+\frac{1}{2}}\Big]. \tag{16}$$

Here $J_{j+\frac{1}{2}}$ and k_1 in equations (15) and (16) are the same as (14b,c). For highly skewed grids and nonuniform flows, equations (6) and (14) are preferred over (15) and (16). However, (14) and (15) do not preserve freestream whereas equations (6) and (16) do. All of the results present in section V use (15). One of the blunt-body cases was rerun with equation (6) and (14)-(16) and no noticeable difference was observed. We expect all of the conclusions on the behavior of (14)-(16) to be carried over to equation (6), since all of the examples use mildly clustered yet quite regular and nearly orthogonal grids.

In two dimensions the present pseudo finite volume formulations can be made 'truly' finite volume by a slight modification of equations (14)-(16); i.e., on the treatment of k_1 and $J_{j+\frac{1}{2}}$. However, the situation is different in three dimensions where finite volume formulations depart from finite difference formulations. See reference [28] for a discussion.

2. The numerical results and conclusions are for the non-MUSCL approach and for the particular flow type and geometry specified with a sampling of a narrow range of Mach numbers and time steps. Results for viscous flow calculations are based on the shock wave dominated thin-layer Navier-Stokes equations for laminar flows.

3. The numerical boundary condition treatments are the same as in references [5,29,30] for the inviscid flow and as in reference [21] for the viscous flows. Studies [31] showed that proper treatment of numerical boundary conditions has a major impact on the stability and convergence rate of the scheme. Therefore the types of boundary condition treatment used here reflect on the performance of the stability, accuracy and convergence rate of the present algorithm.

4. For steady-state computations, the convergence rate not only depends on all of the elements and parameters (to be discussed shortly), but more importantly also on the type of grid associated with the computation. Studies show that, in general, a coarse nearly uniform orthogonal grid converges 1-3 times faster than a similar finer grids, and possibly an order of magnitude or more faster than highly clustered or skewed grids. What will be presented in section V represents fairly uniform to mildly clustered grids. Most of the grids used for the numerical study were not very coarse; thus the number of iterations quoted is naturally higher than its coarse grid counterpart.

5. For the non-interfering blunt-body flows, the convergence rate and behavior of the symmetric and upwind TVD-type schemes are very similar. However, for the interfering blunt-body flows containing slip or shear surfaces, the upwind scheme produces sharper weak solutions. Consequently, all of the illustrations and conclusions discussed in this paper are for the upwind scheme using limiter (9c). Other limiters can produce sharper discontinuities but are not as robust as limiter (9c). See section V or reference 12 for a discussion.

6. Research on real gas effects on the performance of the proposed scheme is only in the preliminary stages. All of the illustrations and conclusions for real gases are for invsicid non-interfering blunt-body flows. Study of viscous real gas flows is in progress.

7. For steady-state computations using the backward Euler time differencing ($\theta = 1$, $\omega = 0$), a local time stepping procedure similar to [30,32] was used. However, in comparing the convergence rate with the three-point backward differentiation time differencing ($\theta = 1$, $\omega = 1/2$) for the viscous flows, a constant time step was used.

Other considerations such as reducing ADI factoring error, using multigrid, relaxation or conjugate gradient methods as an alternative to ADI, using local grid refinement to enhance resolution, etc., are also sources of improvement to algorithm (6-16). These items and the development of better algorithms are the subject of on-going research.

III. Enhancement of Stability and Convergence Rate for Hypersonic Flows

In reference [1], some elements and parameters which can affect the stability and convergence rate in high Mach number cases but have negligible effect in low Mach number cases for steady-state inviscid blunt-body flows were identified. The current study indicated that the same elements and parameters can affect the stability and convergence rate at hypersonic speeds for viscous computations as well. They are as follows: (1) the choice of the entropy correction parameter δ_1, (2) the choice of the dependent variables on which the limiters are applied, and (3) the prevention of unphysical solutions during the initial transient stage.

1. For Mach number ranging from 1.2 to 15, numerical experiments for one- and higher-dimensional unsteady flows containing unsteady shocks show that the second-order explicit TVD schemes [29,12,11] are insensitive to the entropy correction for $0 \leq \delta_1 \leq 0.1$. In most cases $\delta_1 = 0$ was used. For $0.1 \leq \delta_1 \leq 0.25$, there is a possibility of improving stability in the sense of allowing a higher CFL number at the expense of a slight smearing of the discontinuities. However, for unsteady complex shock wave interactions, a small positive δ_1 or a variable δ_1 (to be discussed) can help stabilize the time-accurate implicit algorithm (12).

For subsonic to low supersonic steady-state NACA 0012 airfoil computations [5,6], the resolution of the shock waves was found to be quite insensitive to $0.1 \leq \delta_1 \leq 0.125$ and a constant value seems to be sufficient. However, for hypersonic flows, especially for blunt-body flows, a constant δ_1 or a variable δ_1 suggested by Harten and Hyman [33] was found to be insufficient, but a variable δ_1 depending on the spectral radius of the Jacobian matrices of the fluxes is very helpful in terms of stability and convergence rate. In fact, a proper choice of the entropy parameter δ_1 for higher Mach number flows not only helps in preventing nonphysical solutions but can act, in some sense, as a control of the convergence rate and of the sharpness of shocks and slip surfaces (or shear layer in viscous flows). The smaller the δ_1 that is used, the slower is the convergence rate. The larger the δ_1 that is being used, the larger is the numerical dissipation being added. However, δ_1 cannot be arbitrarily large.

For the present blunt-body steady-state calculations with Mach numbers $M > 4$, the initial flow conditions at the wall are obtained using the known wall temperature in conjunction with pressures computed from a modified Newtonian expression [34]. Also, for implicit methods a slow startup procedure from initial conditions [30] is necessary. Most importantly, experience indicates that if one sets δ_1 in equation (7b) as a function of the velocity and sound speed, i.e.,

$$(\delta_1)_{j+\frac{1}{2}} = \widetilde{\delta}(|u_{j+\frac{1}{2}}| + |v_{j+\frac{1}{2}}| + c_{j+\frac{1}{2}}) \tag{17a}$$

$$(\delta_1)_{k+\frac{1}{2}} = \widetilde{\delta}(|u_{k+\frac{1}{2}}| + |v_{k+\frac{1}{2}}| + c_{k+\frac{1}{2}}) \tag{17b}$$

with $0.05 \leq \widetilde{\delta} \leq 0.25$, then blunt-body flows for $4 \leq M \leq 25$ appear to be stabilized and nonphysical solutions are less likely to occur. Equation (17) is written in Cartesian coordinates. In the case of generalized coordinates, the u and v should be replaced by the contravariant velocity components, and one half of the sound speed would be from the ξ-direction and the other half would be from the η-direction. For implicit methods, it is very important to use (17) in $\psi(z)$ on both the implicit and explicit operators since in a two-dimensional hypersonic flow field consisting of a mixture of subsonic and supersonic regions with Mach number ranging from 0 to hypersonic speeds, an entropy parameter like (17) is nonzero in all of the regions. The entropy parameter (17) seems to work well for blunt-body flows but whether this is also the right choice for configurations other than a blunt-body shape is an open question.

For unsteady hypersonic blunt body complex shock wave interactions, the entropy parameter (17) can help stabilize the time-accurate implicit algorithm. For most of the viscous and inviscid calculations shown, unless otherwise indicated, $\widetilde{\delta}$ is set to 0.125.

2. Higher-order TVD schemes in general involve limiter functions. However, there are options in choosing the types of dependent variables when applying limiters for systems of hyperbolic conservation law, in particular for systems in generalized coordinates. The choice of the dependent variables on which limiters are applied can affect the convergence process. In particular, due to the nonuniqueness of the eigenvectors $R_{j+\frac{1}{2}}$, the choice of the characteristic variables on which the limiters are applied play an important role in the convergence rate as the Mach number increases. For moderate Mach numbers, the different choices of the eigenvectors have a negligible effect on the convergence rate. However, for large Mach number cases, the magnitudes of all the variables at the jump of the bow shock are not the same. In general, the jumps are much larger for the pressures than for the densities or total energy. Studies indicated that employing the form $R_{j+\frac{1}{2}}$ such that the variation of the α are of the same order of magnitude as the pressure would be a good choice for hypersonic flows. The form similar to the one used by Gnoffo [35] or Roe and Pike [36] can improve the convergence rate over the ones used in references [37,38]. In all of the computations shown the form $R_{j+\frac{1}{2}}$ used is the same as in references [37,38] except for an extra factor of $1/c^2_{j+\frac{1}{2}}$. With this extra factor the variation of the α are in fact proportional to the pressure. Other forms of $R_{j+\frac{1}{2}}$ have not been investigated.

3. Due to the large gradients and to the fact that the initial conditions are far from the steady-state physical solution, the path used by the implicit method can go through states with negative pressures if a large time step is employed. A convenient way to overcome this difficulty is to fix a minimum non-negative allowed value for the density and the pressure. With this safety check, the scheme allows a much larger time step and converges several times faster.

In addition, since the Roe's average state allows the square of the average sound speed $c^2_{j+\frac{1}{2}}$ to lie outside the interval between c^2_j and c^2_{j+1}, the average state $c^2_{j+\frac{1}{2}}$ might be negative even though c^2_j

and c^2_{j+1} are positive during the transient stage when the initial conditions are far from the steady-state physical solution. In this case, we replace $c^2_{j+\frac{1}{2}}$ by $\max(c^2_{j+\frac{1}{2}}, \min(c^2_j, c^2_{j+1}))$. This latter safety check is in particular helpful for the symmetric TVD algorithm (7).

IV. Behavior of the Algorithm with Different Temporal Differencing

It is emphasized here that since the method (12) is written in the 'delta' formulation, either the backward Euler (first-order) or the three-point backward differentiation (second-order) time discretizations require the same amount of storage and a similar operation count. Therefore, the main consideration between the two time-differencing methods is their relative stability and convergence rate.

Inviscid Unsteady Flows: For inviscid unsteady flows, the explicit TVD-type methods [29,12,11] are more efficient than the second-order implicit method (12). Unless the inviscid problem is stiff, there is no advantage of employing an implicit method for inviscid unsteady flows.

Inviscid Steady Flows: The backward Euler implicit method has a better stability and convergence rate than the three-point backward differentiation implicit method. Also a local time-stepping procedure can speed up the convergence rate for the former time-differencing method whereas the same procedure has little effect on the convergence rate when compared with a fixed time step procedure for the latter time-differencing method.

Viscous Unsteady Flows: Computations on the unsteady viscous flows mainly use the second-order time differencing since a larger time step can be used compared with the temporally first-order implicit method. Due to the highly clustered viscous grid used in contrast to their inviscid counterpart, solving a viscous unsteady complex shock interaction using an explicit TVD-type method is not practical due to its inherent time step restriction. In certain cases, the time step might be an order of magnitude smaller than the implicit counterpart. A more detailed study of unsteady viscous hypersonic blunt-body flows with an impinging shock is reported in reference [22].

Viscous Steady Flows: At present there is no detailed viscous steady flow study comparing the first-order time differencing using a local time-stepping approach with the second-order time differencing using a constant time step approach. But the general trend is that the second-order time differencing has slightly better stability and convergence rate than the former one. In particular, a summary using a fixed time step approach comparing the two time-differencing algorithms is discussed in section V.

V. Numerical Results

The various numerical aspects discussed in sections III-IV are complimented by a variety of steady and unsteady, viscous and inviscid hypersonic blunt-body flow computations in this section. Six types of blunt-body test cases are illustrated in figures 1-11. Test cases 1 and 2 are inviscid, perfect and real gas, non-interfering blunt-body flows. Test case 3 is a steady inviscid, perfect gas blunt-body flow with an impinging shock. Test cases 4-6 are viscous steady and unsteady perfect gas blunt-body flows with and without impinging shocks.

Comparison Among the Various Linearized Implicit Methods: For the implicit operator, numerical experiments show that the linearized conservative form (12) converges slightly faster than the linearized nonconservative form [4] for both viscous and inviscid flows. It seems also that when the freestream Mach number increases, the convergence rate of the linerarized conservative form (12) is better than a simplified version which replaces $\Omega^{\xi}_{j+\frac{1}{2},k}$ and $\Omega^{\eta}_{j,k+\frac{1}{2}}$ of (12g,h) by $\max_l \psi(a^l_{j+\frac{1}{2}})$

and $\max_l \psi(a^l_{k+\frac{1}{2}})$ times the identity matrix (equation (13)). This is especially true for viscous flow computations. Due to the experience gained by the transonic and the inviscid hypersonic study, no detailed computations using the linearized nonconservative form were performed for viscous steady flow. All of the results and discussions for the viscous computations are based on the conservative linearized form.

Another area of investigation is that for viscous computations, the Jacobian of the viscous terms on the implicit operators are rather expensive to compute. To maintain the spatial order of accuracy, for sure these terms are needed for unsteady flows. Whether the omission of these terms has a major impact on the stability and convergence rate of the algorithm for steady-state calculations is not known. Therefore, an investigation has been made on the difference in the convergence rate for the algorithm with or without the viscous terms in the implicit operator. A brief summary is included in the following subsection.

Choice of Limiters: Unlike flows with transonic and low supersonic shock waves, problems containing strong hypersonic shock waves are more sensitive to the treatment of limiters. Using the more diffusive limiter (7c) or (9c) turns out to be more stable than other more compressive limiters. In terms of shock resolution for both the symmetric and upwind TVD-type of schemes, the sequences written in equations (7c)-(7e) and (9c)-(9g) are in order of increasing accuracy. On the other hand, these sequences are in order of decreasing stability and convergence rate. The more compressive limiters like (9f) and (9g) have a very low stability and slow convergence rate for steady flows. The same conclusion applies for unsteady flows where the more compressive limiters have a very restricted time step limit. From our experiences, it is not advisable to use (9f) and (9g) for complex steady shock wave interactions. In particular, limiter (9g) should be used only for the linear fields (i.e., for the u and v characteristic fields in the x- and y-direction respectively). See reference [12] for more details.

Convergence Rate of Explicit and Implicit TVD-type Schemes for Real Gas Flows: The five different second-order TVD methods previously studied [11] in one dimension yield very similar shock resolution for the blunt-body (non-interfering case) problem. In particular, for an inviscid blunt-body flow in the hypersonic equilibrium real gas range, the explicit second-order Harten and Yee, and Yee-Roe-Davis type TVD schemes [6,24,25] using the generalized approximate Riemann solver [13] produce similar shock-resolution but converge slightly faster than an explicit second-order van Leer type scheme using the generalized van Leer flux-vector splitting [11].

The freestream conditions for the current study are $M_\infty = 15$ and 25, $p_\infty = 1.22 \times 10^3\ N/m^2$, $\rho_\infty = 1.88 \times 10^{-2}\ kg/m^3$, and $T_\infty = 226°$K. Figure 1 shows half of the 61×33 grid used for the blunt-body problem. For the $M_\infty = 25$ case, the shock stand off distance is at approximately fourteen points from the wall on the symmetry axis. The relaxation procedure for the explicit methods employs a second-order Runge-Kutta time discretization with a CFL of 0.5 (solution not shown). The parameter $\tilde{\delta}$ is set to a constant value of 0.15. Pressure and Mach number contours converge and stabilize after 3000-4000 steps but the convergence rate is much slower for the density (with a 2-3 order of magnitude drop in L_2-norm residual). The bow shock is captured in two to three grid points. The curve fits of Srinivasan et al. [39] are used to generate the thermodynamic properties of the gas.

The same flow condition was tested on the implicit scheme (12) and the convergence rate was found to be many times faster. Figures 2 and 3 show the Mach number, density, pressure and κ contours computed by the linearized conservative ADI form of the upwind scheme (12) with the first-order backward Euler ($\theta = 1$ and $\omega = 0$) for Mach numbers 15 and 25. Figure 4 shows the

slight advantage of the convergence rate of the linearized conservative implicit scheme (12) over the linearized nonconservative implicit scheme (with $\theta = 1$, $\omega = 0$ and a fixed CFL of 15) suggested in reference [4]. The convergence rate and shock resolution for the symmetric TVD-type scheme (12) behave similarly. For $M_\infty = 15$ case, the L_2-norm residual stagnated after a drop of four orders of magnitude.

In general, for a perfect gas with $10 \leq M_\infty \leq 25$ and a not highly clustered grid, steady-state solutions can be reached in 600-800 steps with 12 orders of magnitude drop in the L_2-norm residual. However, the convergence rate is many times slower for the real gas counterpart. Figure 5 shows the convergence rate for a perfect gas compared with a real gas computation with a fixed CFL of 50. Note that the scale of the ordinates used in figure 5 for the perfect gas and the real gas are not the same. The freestream conditions for the real gas study are the same as figure 3. An important observation for the behavior of the convergence rate for the Mach 15 real gas case is that the discontinuities of the thermodynamic derivatives which exist in the curve fits of Srinivasan et al. [39] might be the major contributing factor. This is evident from figures 2d and 3d and from a comparison with the convergence rate for the perfect gas. Another contributing factor is that the curve fits are accurate only for temperatures up to 6000°K. Since the temperature in this case is slightly above 6000°K, there is an uncertainty in the accuracy of the computed results. Further improvement of the existing curve fitting procedure is needed.

Inviscid Impinging Shock Computations: Figures 6 and 7 show the schematic of the computational domain, the Mach contours and L_2-norm residual computed by the implicit upwind scheme (12) (with $\theta = 1$, $\omega = 0$) of an inviscid shock-on-shock interaction on a blunt body with radius R_l and thickness $D = 2R_l$ in the low hypersonic range. Higher inviscid hypersonic Mach number computations using the proposed scheme are also possible but are not shown here. Some viscous and inviscid studies on flow fields of this type were reported in references [34,40-42]. This flow field is typical of what may be experienced by the inlet cowl of a hypersonic aerodynamic vehicle. The freestream conditions for this flow field are the freestream Mach number $M_\infty = 4.6$, the freestream temperature $T_\infty = 167$°K, and $\gamma = 1.4$ for a perfect gas. An oblique shock with an angle of 20.9° relative to the free stream impinges on the bow shock. Various types of interactions occur depending on where the impingement point is located on the bow shock. As shown by the Mach contours ranging from 0 to 4.55 in increments of 0.05, the impinging shock has caused the stagnation point to move away from its undisturbed location at the symmetry line. The surface pressures at the new stagnation point can be several times larger than those at the undisturbed location of the stagnation point. In addition, a slip surface emanates from the bow shock and impinging shock intersection point and is intercepted by a shock wave which starts at the upper kink of the bow shock. The interacting shock waves and slip surfaces are confined to a very small region and must be captured accurately by the numerical scheme if the proper surface pressures are to be predicted correctly. The 77 × 77 grid used and the convergence rate computed by the implicit scheme (12) are shown in figure 7. Though the pattern of the flow is significantly more complicated than for the previous cases, the convergence rate remains quite satisfactory. As shown in figure 6 at the inflow, all of the inviscid and viscous interfering blunt-body computations start with the appropriate freestream and oblique shock wave conditions as boundary conditions.

Viscous Steady Computations With or Without Impinging Shock: To keep the study tractable only two types of physical flow fields were chosen. The first is the viscous hypersonic blunt-body flow at $M_\infty = 8.03$ and $T_\infty = 122.1$°K with a laminar Reynolds number of 387,750 based on the body diameter for ideal gases. The second problem (with the same flow conditions) is similar to the inviscid shock-on-shock interaction where an oblique shock impinges on the bow shock of the blunt body at an angle of 19° relative to the free stream. A more detailed flow field computation on the six types of shock patterns categorized by Edney [43] is presented in reference [21]. For the convergence

study only one type of interaction, namely what is called the Type III interaction, is considered. Also the study is restricted to only one type of time stepping sequencing and only one value of the entropy correction parameter. The computational meshes (not shown) consist of 181 points in the circumferential direction and 91 points in the normal to the body direction and are highly clustered in the wall region to resolve the viscous layer.

At this point, it is important to point out that the time step sequence used for the viscous steady flows is very different from the inviscid study. Most of the inviscid computations use the same initial time step input together with a local time-stepping procedure throughout the entire iteration process. The time step sequence chosen for the viscous steady calculations is based on experience with a wide range of hypersonic flow simulations and consists of doubling the time step every 100-400 time steps until the specified time step is reached. The initial time step is $\Delta t = 0.001$ which corresponds to a maximum Courant (CFL) number of 10 to 20 for the current problem and grid size. Larger values of the initial time step usually prevent convergence. The four specified time steps considered range from 0.001 to 0.008 with the corresponding CFL numbers ranging from 20 to 200. Much larger maximum CFL (or specified time step) numbers are possible but do not improve the convergence rates. The value of the entropy correction parameter was fixed at $\tilde{\delta} = 0.15$, again based on experience with a wide range of hypersonic flow field simulations.

The results of the blunt-body steady viscous flow obtained with the temporally second-order accurate algorithm (12) (hereafter referred to as the full matrix form) are shown in figure 8. Here algorithm (12) for the viscous computations means the appropriate three-point central differences of the viscous terms are added to the explicit and implicit operators of (12). Depicted are the Mach contours ranging from 0 to 8 in increments of 0.1 and the entropy contours normalized with the freestream value and ranging from 0 to 6.4 in increments of 0.1. The final view in figure 8 is the L_2 norm residual history. The residual drops to machine accuracy (10^{-14}) in less than 3200 steps. The corresponding results using the same algorithm (12a)-(12f) together with (13) (hereafter referred as the diagonal form) are illustrated in figure 9. No noticeable difference in the numerical results is observed in the Mach number or entropy contours. However, the residual curves are very different. The residual for the diagonal scheme reached a plateau of 5×10^{-6} at 1500 steps and stayed at that level.

A more difficult flow field computation is depicted in figures 10 and 11. The results using the same second-order time accurate full matrix algorithm are shown in figure 10. The convergence rate is slower than for the blunt body non-interfering case but is still satisfactory. The residual dropped seven orders of magnitude in 3000 steps. In both of the blunt-body flow with or without impinging shocks, steady-state can be reached within 1000-1500 iterations. The extra iterations are needed only to bring the residual to a lower level but no change in the coutour plots or surface pressures at least to within 3-4 digits of accuracy is observed. However, the results shown in figure 11 using the diagonal scheme are not satisfactory. The residuals dropped less than two orders of magnitude in 3000 steps. The noise appearing on the Mach number and entropy contours in the upper portion of the bow shock using the diagonal form of the scheme indicates that the algorithm has a problem reaching the converged steady-state solution.

All of the results obtained for figures 8-11 have the viscous terms included in the implicit operator. If the viscous terms are not included in the impicit operator, then the full matrix scheme becomes unstable for $\Delta t \geq 0.004$, whereas the diagonal scheme exhibits no change in convergence rate.

In summary, from the point of view based on the L_2-norm of the residuals, the best convergence rates were achieved by the full matrix form with the viscous terms included since it allowed the residual to drop to machine accuracy (10^{-14}). The diagonal form (13) did not fare too well. Although there is a substantial savings in operation count per iteration, the L_2-norm of the residual never

dropped below 10^{-6} for all the time steps considered. Moreover, the inclusion of the implicit viscous terms had little effect on the diagonal form of the scheme but is important for the full matrix form of the scheme. One way of taking advantage of the low operations count of the diagonal form (without the implicit viscous terms) is to use the scheme as an efficient way of obtaining a rough solution (from freestream) for the initial input to the full matrix algorithm. The temporally second-order time-differencing scheme had a marginal but beneficial effect on the convergence rates when compared with the temporally first-order scheme.

Viscous Steady and Unsteady Mach 15 Computations With Impinging Shock: Figure 12 illustrates the shock resolution of unsteady and steady thin-layer Navier-Stokes computations by the second-order time-accurate, full matrix algorithm (12). This steady test case is similar to the previous impinging shock study except the freestream Mach number is 15, the impingement shock angle is 22.75°, the freestream temperature is T_∞ = 255.6°K, and the Reynolds number based on the diameter is 186,000. Shown are the Mach contours from 0 to 15 in increments of 0.1. For the unsteady computation, the impingement shock at an angle of 22.75° relative to the freestream moves downward across the bow-shock of the blunt body. The impingement shock velocity is 10% of the freestream velocity (M_∞ = 15). Although the impingement shock locations for the unsteady and steady computations are similar, the shock patterns are very different. A 241 × 141 non-adaptive grid is used for both computations. A time step of 0.002 (equivalent to a maximum CFL of 48) is used for steady-state computations whereas a time step of 0.0005 (equivalent to a maximum CFL of 10-12 at the vicinity of the boundary layer and a CFL of 1 at the rest of the flow field) is used for the unsteady computations. The steady-state solution can be reached in 1200 steps with a three order of magnitude drop in the L_2-norm residual. More detailed study of the surface pressure and heat transfer rate of these types of shock-on-shock steady and unsteady numerical simulations were reported in references [21,22].

VI. Concluding Remarks

A two-parameter family of implicit time-accurate shock-capturing algorithms for hypersonic viscous flows has been developed. The proposed algorithms are formulated in finite volume and pseudo finite volume form and have been shown to be quite efficient and accurate for steady-state as well as unsteady viscous and inviscid hypersonic complex shock interactions. Some numerical aspects of these TVD-type algorithms that affect the convergence rate for hypersonic Mach numbers or real gas flows but have negligible effect on low Mach numbers or perfect gas flows are identified. Improvements have been made to the algorithms to speed up the convergence rate in the hypersonic flow regime. Even with the improvements, though, the convergence is in general slower for real gases than for a perfect gas. The nonsmoothness in the curve fits of Srinivasan et al. may be a major contributing factor in slowing down the convergence rate. Also, the convergence rate is, in general, slower for viscous flows than for inviscid steady flows.

References

[1] Montagne, J.-L., Yee, H.C., Klopfer, G.H. and Vinokur, M., "Hypersonic Blunt Body Computations Including Real Gas Effects," Proceedings of the 2nd International Conference in Hyperbolic Problems, March 14-18, 1988, Aachen, Germany, also NASA TM-100074, March 1988.

[2] Yee, H.C. and Shinn, J.L., "Semi-implicit and Fully Implicit Shock-Capturing Methods for Hyperbolic Conservation Laws with Stiff Source Terms," AIAA-87-1116-CP, Proceedings of the AIAA 8th Computational Fluid Dynamics Conference, June 9-11, 1987, Honolulu, Hawaii, pp. 159-176.

[3] LeVeque, R.J. and Yee, H.C., "A Study of Numerical Methods for Hyperbolic Conservation Laws with Stiff Source Terms," NASA TM-100075, March 1988.

[4] Yee, H.C., "Linearized Form of Implicit TVD Schemes for the Multidimensional Euler and Navier-Stokes Equations," *Computers and Mathematics with Applications*, Vol. 12A, No. 4/5, 1986, pp. 413-432.

[5] Yee, H.C. and Harten, A., "Implicit TVD Schemes for Hyperbolic Conservation Laws in Curvilinear Coordinates," AIAA Paper No. 85-1513, Proceedings of the AIAA 7th CFD conference, Cinn., Ohio, July 1985; also *AIAA Journal*, Vol. 25, No. 2, 1987, pp. 266-274.

[6] Yee, H.C., "Construction of Explicit and Implicit Symmetric TVD Schemes and Their Applications," *Journal of Computational Physics*, Vol 68. 1987 pp. 151-179; also NASA TM-86775 July 1985.

[7] van Leer, B., "Towards the Ultimate Conservation Difference Scheme V, A Second-Order Sequel to Godunov's Method," *Journal of Computational Physics* Vol. 32, 1979, PP. 101-136.

[8] Anderson, K.W., Thomas, J.L. and van Leer, B., "A Comparison of Finite Volume Flux Vector Splittings for the Euler Equations," *AIAA Journal*, Vol. 24, No. 9, September 1986, pp. 1453-1460.

[9] Osher, S. and Chakravarthy, S., "Very High Order Accurate TVD Schemes," *The IMA Volumes in Mathematics and Its Applications*, Vol. 2, Springer-Verlag, 1986, pp. 229-274.

[10] Woodward, P. and Colella, P., "The Numerical Simulation of Two-Dimensional Fluid Flows with Strong Shocks," *Journal of Computational Physics*, Vol. 54, 1984, pp. 115-173.

[11] Montagné, J.-L., Yee, H.C. and Vinokur, M., "Comparative Study of High-Resolution Shock-Capturing Schemes for Real Gas," Proceeding of the 7th GAMM conference on Numerical Methods in Fluid Mechanics, Sept. 9-11, 1987, Belgium, also NASA TM-86839, July 1987.

[12] Yee, H.C., "Upwind and Symmetric Shock-Capturing Schemes," NASA TM-89464, May, 1987, also to appear, proceedings of the *Seminar on Computational Aerodynamics*, Dept. Mech. Engin., University of Calif., Davis, Spring Quarter, 1986.

[13] Roe, P.L., "Approximate Riemann Solvers, Parameter Vectors, and Difference Schemes," *Journal of Computational Physics*, Vol. 43, 1981, pp. 357-372.

[14] Vinokur, M., "Generalized Roe Averaging for Real Gas," NASA Contractor Report, in preparation.

[15] Vinokur, M. and Liu, Y., "Equilibrium Gas Flow Computations II. An Analysis of Numerical Formulations of Conservation Laws," AIAA-88-0127, January 1988, Reno, Nevada.

[16] Steger, J.L. and Warming, R.F., "Flux Vector Splitting of the Inviscid Gasdynamic Equations with Application to Finite Difference Methods," *Journal of Computational Physics*, Vol. 40, No. 2, 1981, pp. 263-293.

[17] van Leer, B., "Flux-Vector Splitting for the Euler Equations," ICASE Report No. 82-30, Sept. 1982.

[18] Vinokur, M. and Montagné, J.-L., "Generalized Flux-Vector Splitting for an Equilibrium Gas," NASA contractor report, in preparation.

[19] Harten, A., "On a Class of High Resolution Total-Variation-Stable Finite-Difference Schemes," *SIAM Journal of Numerical Analysis*, Vol. 21, 1984, pp. 1-23.

[20] Takakura, Y., Ishiguro, T. and Ogawa, S., On the Recent Difference Schemes for Three-Dimensional Euler Equations," AIAA-87-1151-CP, Proceedings of the AIAA 8th Computational Fluid Dynamics Conference, June 9-11, 1987, Honolulu, Hawaii, pp. 537-545.

[21] Klopfer, G. and Yee, H.C., "Viscous Hypersonic Shock on Shock Interaction on Blunt Cowl Lips," AIAA-88-0233, AIAA 26th Aerospace Sciences Meeting, Jan. 11-14, 1988, Reno, Nevada.

[22] Klopfer, G, Yee, H.C. and Kutler, P., "Numerical Study of Unsteady Viscous Hypersonic Blunt Body Flows With An Impinging Shock," Proceedings of the 11th International Conference on Numerical Methods in Fluid Dynamics, June 27 - July 1, 1988, Williamsburg, Virginia, also NASA TM-100096, April 1988.

[23] Roe, P.L., "Some Contributions to the Modelling of Discontinuous Flows," *Lectures in Applied Mathematics*, Vol. 22 (Amer. Math. Soc., Providence, R.I., 1985), pp. 163-194.

[24] Roe, P.L., "Generalized Formulation of TVD Lax-Wendroff Schemes," ICASE Report No. 84-53, Oct. 1984.

[25] Davis, S.F., "TVD Finite Difference Schemes and Artificial Viscosity," ICASE Report No. 84-20, June, 1984.

[26] Yee, H.C., "On the Implementation of a Class of Upwind Schemes for System of Hyperbolic Conservation Laws," NASA TM-86839, Sept. 1985.

[27] Barth, T.J., "Analysis of Implicit Local Linearization Techniques for Upwind and TVD Algorithms," AIAA-87-0595, Reno, Nevada, 1987.

[28] Vinokur, M., "An Analysis of Finite-Difference and Finite-Volume Formulations of Conservation Laws," NASA Contractor Report 177416, June 1986.

[29] Yee, H.C., "Numerical Experiments with a Symmetric High-Resolution Shock-Capturing Scheme," Proc. 10th Int. Conf. on Numerical Methods in Fluid Dynamics, June 1986, Beijing, China, also NASA TM-88325, June, 1986.

[30] Pulliam, T.H. and Steger, J.L., "Recent Improvements in Efficiency, Accuracy and Convergence for Implicit Approximate Factorization Algorithms," AIAA Paper 85-0360, 1985.

[31] Yee, H.C., "Numerical Approximation of Boundary Conditions with Applications to Inviscid Equations of Gas Dynamics," NASA TM-81265, 1981.

[32] Jameson, A., Schmidt, W. and Turkel, E., "Numerical Solutions of the Euler equations by Finite Volume Methods Using Runge-Kutta Time-Stepping Schemes," AIAA Paper 81-1259, 1981.

[33] Harten, A. and Hyman, J.M., "A Self-Adjusting Grid for the Computation of Weak Solutions of Hyperbolic Conservation Laws," *Journal of Computational Physics*, Vol. 50, 1983, pp. 235-269.

[34] Tannehill, J.C., Holst, T.L., and Rakich, J.V. "Numerical Computation of Two-Dimensional Viscous Blunt Body Flows with an Impinging Shock," *AIAA Journal*, Vol. 14, No. 2, February 1976.

[35] Gnoffo, P.A. and McCandless, R.S., "Three-Dimensional AOTV Flowfields in Chemical Nonequilibrium," AIAA Paper 86-0230, Jan. 1986.

[36] Roe, P.L. and Pike, J., "Efficient Construction and Utilisation of Approximate Riemann Solutions, Computing Methods in Applied Sciences and Engineering, ed. R. Glowinski, North-Holland, Amsterdam, J.-L. Lions, 1984, pp. 499-518.

[37] Yee, H.C., Warming, R.F. and Harten, A., "Implicit Total Variation Diminishing Schemes (TVD) for Steady-State Calculations," *Journal of Computational Physics*, Vol. 57, No. 3, 1985, pp. 327-360.

[38] Yee, H.C. and Kutler, P., "Application of Second-Order-Accurate Total Variation Diminishing (TVD) Schemes to the Euler Equations in General Geometries," NASA TM-85845, August 1983.

[39] S. Srinivasan, J.C. Tannehill, K.J. Weilmunster, "Simplified Curve Fit for the Thermodynamic Properties of Equilibrium Air," ISU-ERI-Ames 86401; ERI Project 1626; CFD15.

[40] Tannehill, J.C., Holst, T.L., Rakich, J.V., and Keyes, J.W., "Comparison of a Two-Dimensional Shock Impingement Computation with Experiment," *AIAA Journal*, Vol. 14, No. 4, April 1976.

[41] White, J.A., and Rhie, C.M., "Numerical Analysis of Peak Heat Transfer Rates for Hypersonic Flow over a Cowl Leading Edge," AIAA-87-1895, June 1987.

[42] Morgan, K., Peraire, J., Thareja, R.R., and Stewart, J.R., "An Adaptive Finite Element Scheme for the Euler and Navier-Stokes Equations", AIAA-87-1172-CP, Proceedings of the AIAA 8th Computational Fluid Dynamics Conference, June 9-11, 1987, Honolulu, Hawaii, pp. 749-757.

[43] Edney, B.E., "Anomalous Heat Transfer and Pressure Distributions on Blunt Bodies at Hypersonic Speeds in the Presence of an Impinging Shock," FFA Report 115, February 1968, The Aeronautical Research Institute of Sweden, Stockholm, Sweden.

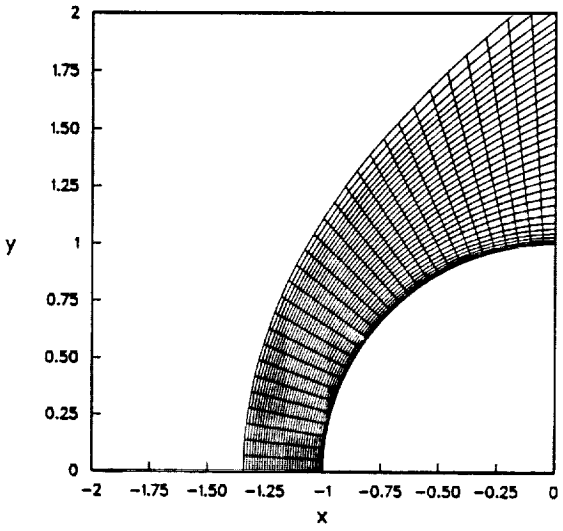

Fig. 1 The 31 × 33 grid.

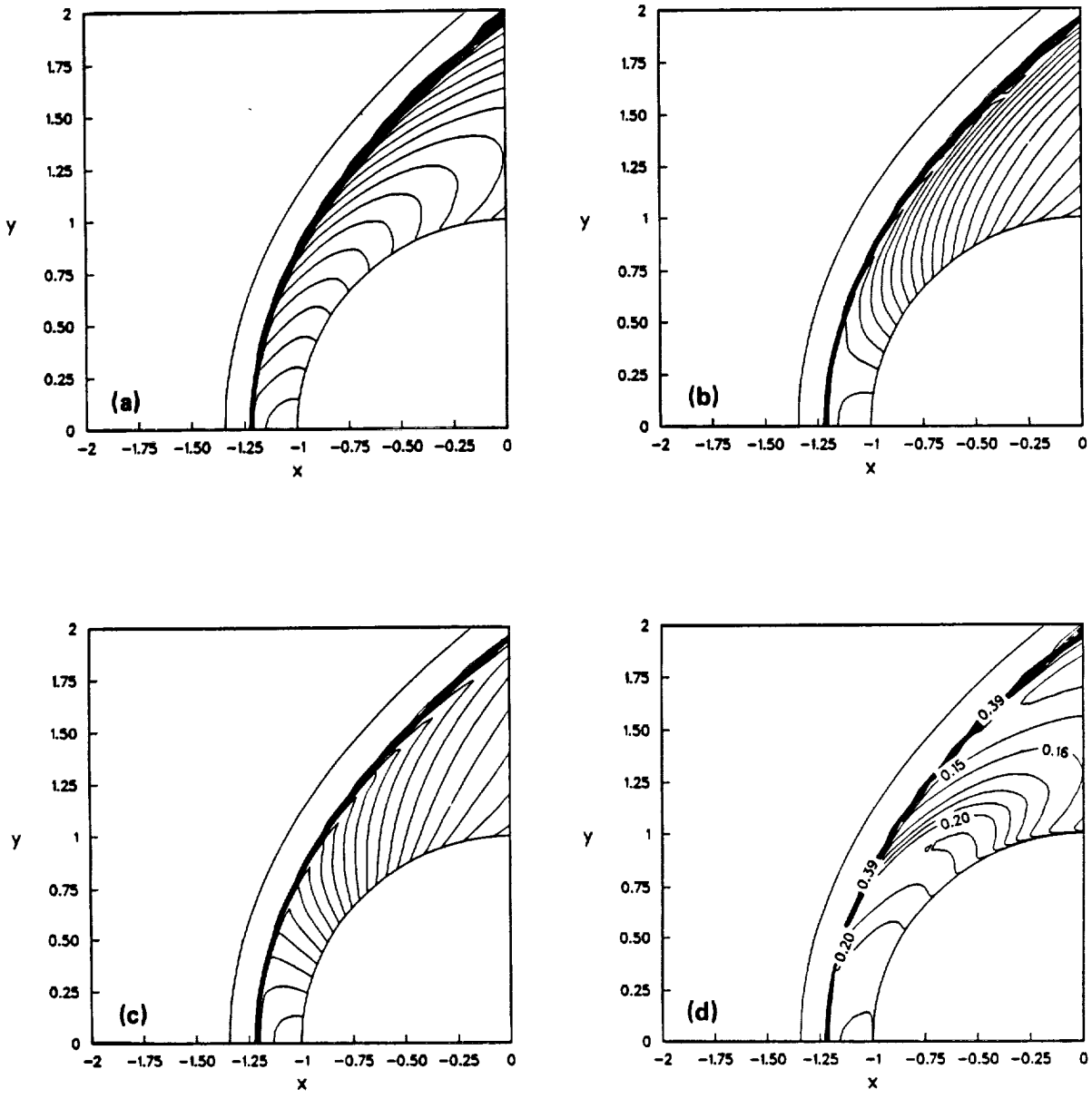

Fig. 2 The Mach contours (a), density contours (b), pressure contours (c) and κ (d) computed by the implicit scheme (12) ($\theta = 1$, $\omega = 0$) for an equilibrium real gas with $M_\infty = 15$.

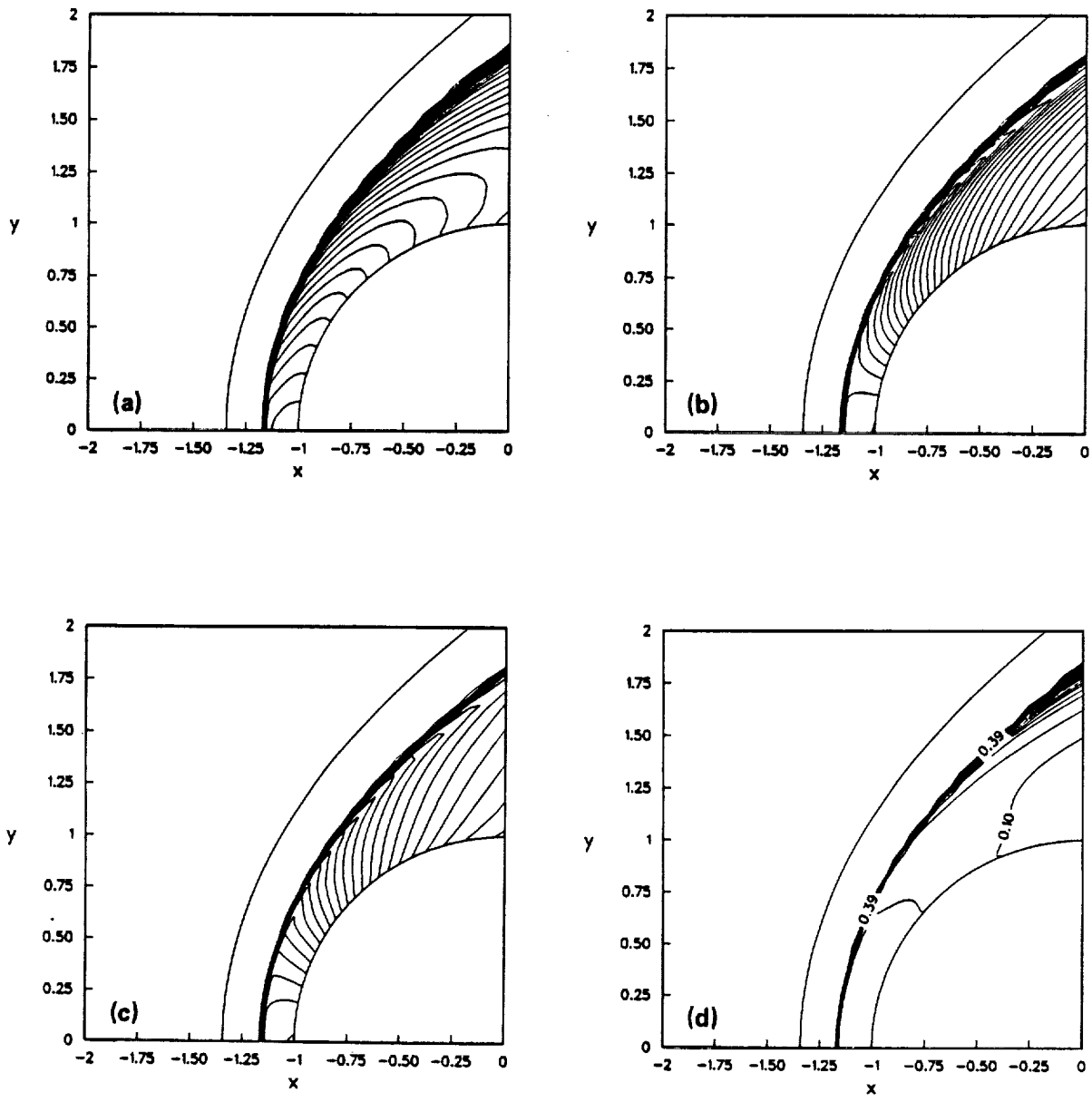

Fig. 3 The Mach contours (a), density contours (b), pressure contours (c) and κ (d) computed by the implicit scheme (12) ($\theta = 1$, $\omega = 0$) for an equilibrium real gas with $M_\infty = 25$.

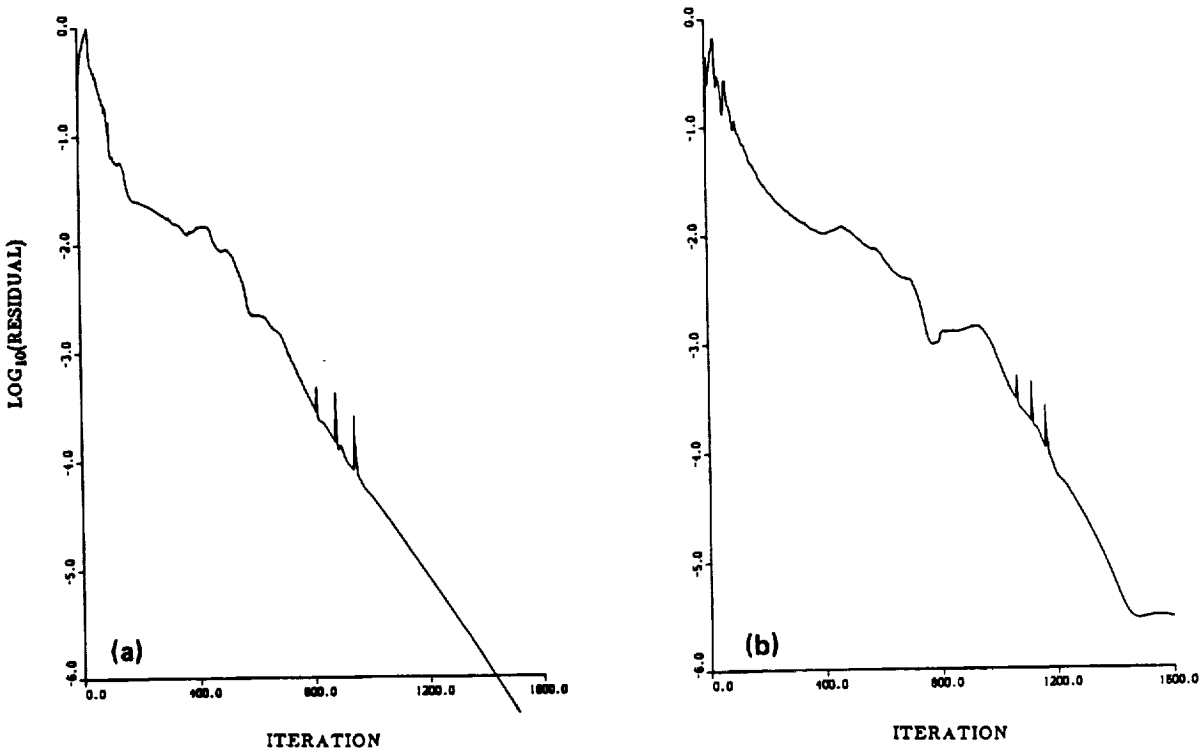

Fig. 4 Comparison of the L_2-norm residual of a linearized conservative implicit operator (a) and a linearized nonconservative implicit operator (b) for an equilibrium real gas with $M_\infty = 25$.

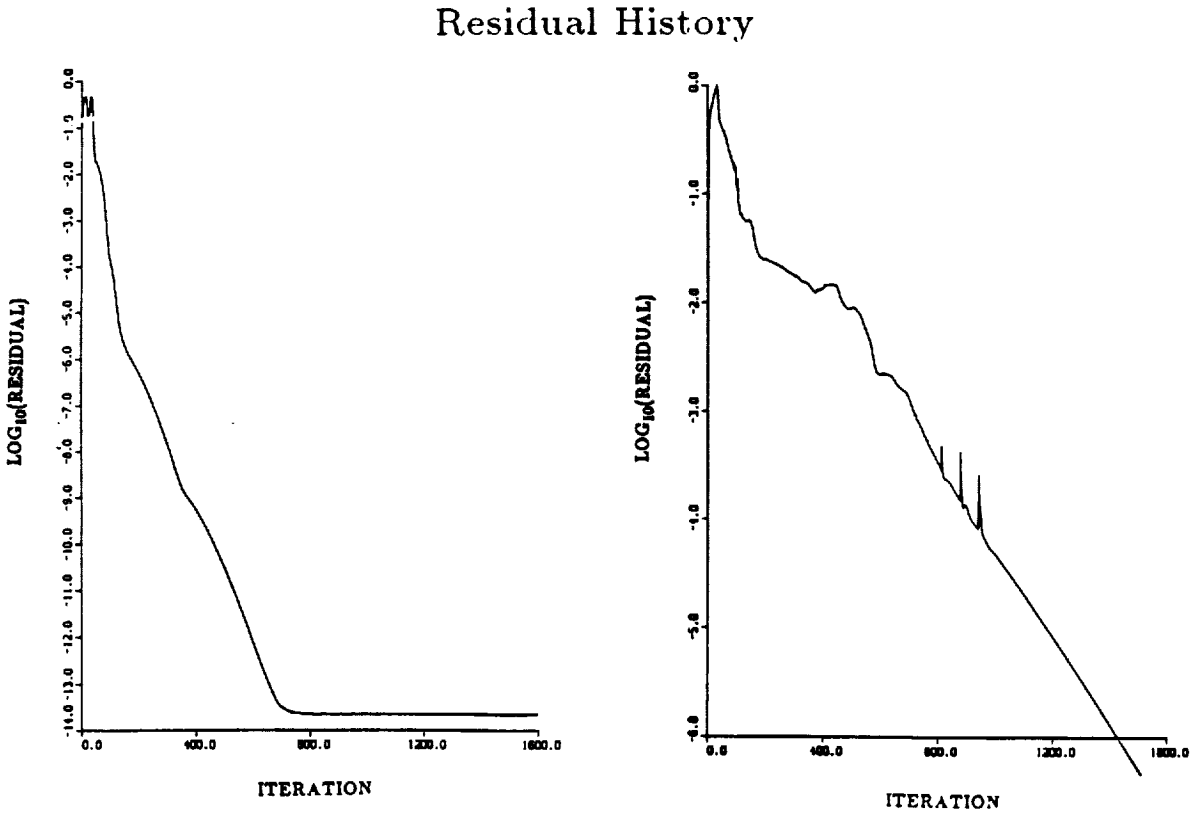

Fig. 5 Comparison of the L_2-norm residual of a perfect gas and real gas computed by the scheme (12) ($\theta = 1$, $\omega = 0$) with $M_\infty = 25$. Note that the scale of the ordinate for the perfect gas and the real gas is not the same.

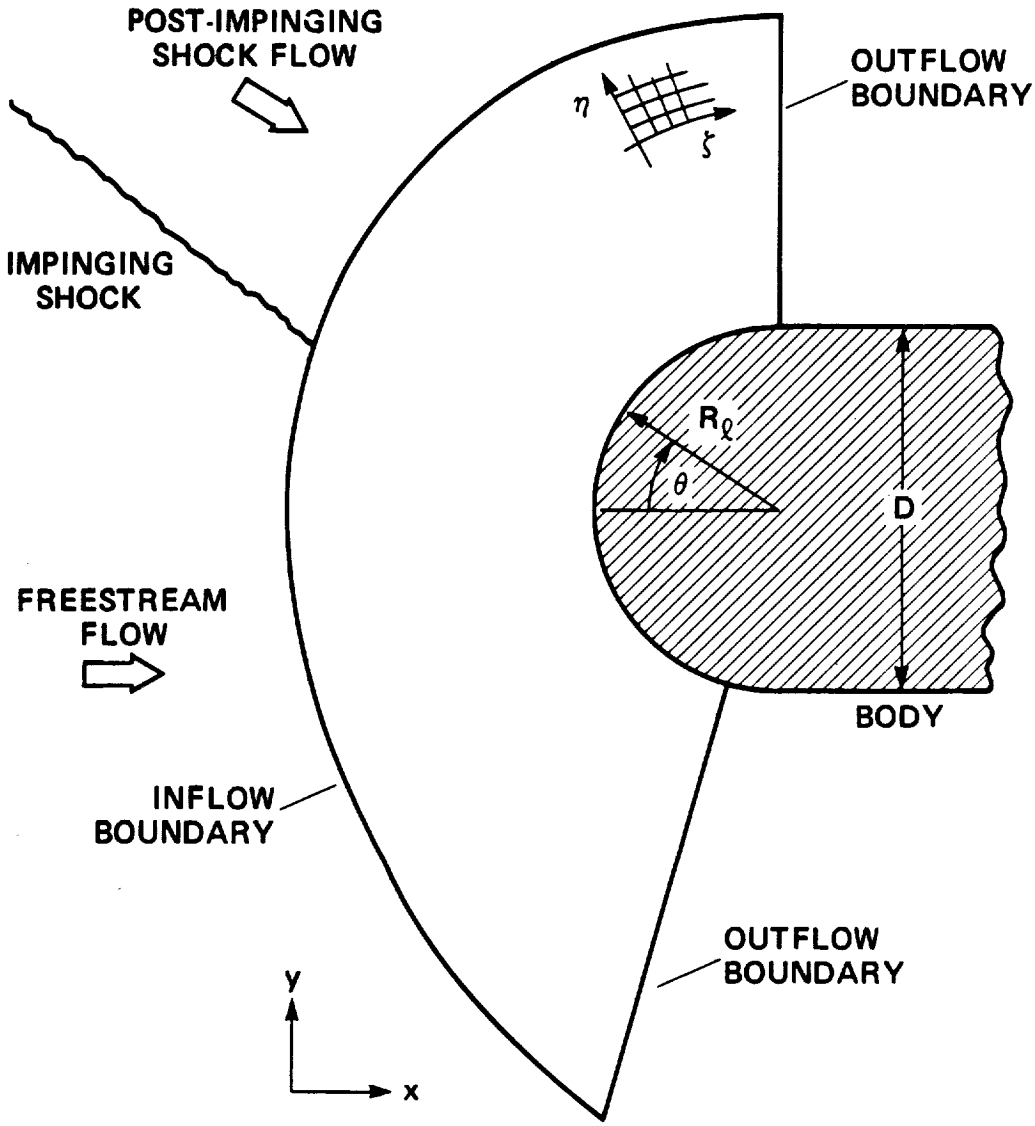

Fig. 6 Schematic of the computational domain for a blunt body flow with an impinging shock.

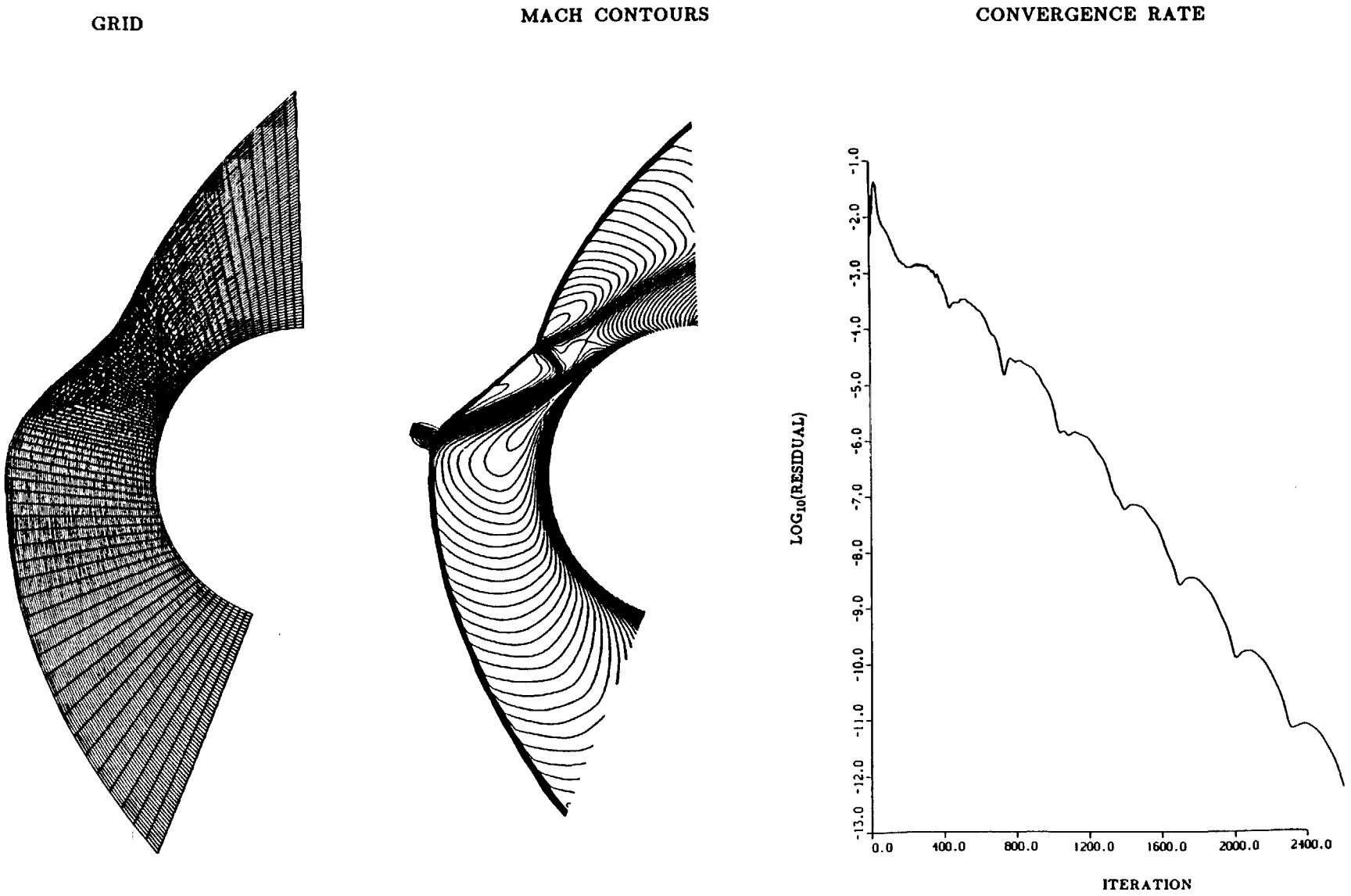

Fig. 7 Two-dimensional inviscid steady blunt-body flow with an impinging shock computed by the implicit scheme (12) ($\theta = 1$, $\omega = 0$) for a perfect gas with $M_\infty = 4.6$.

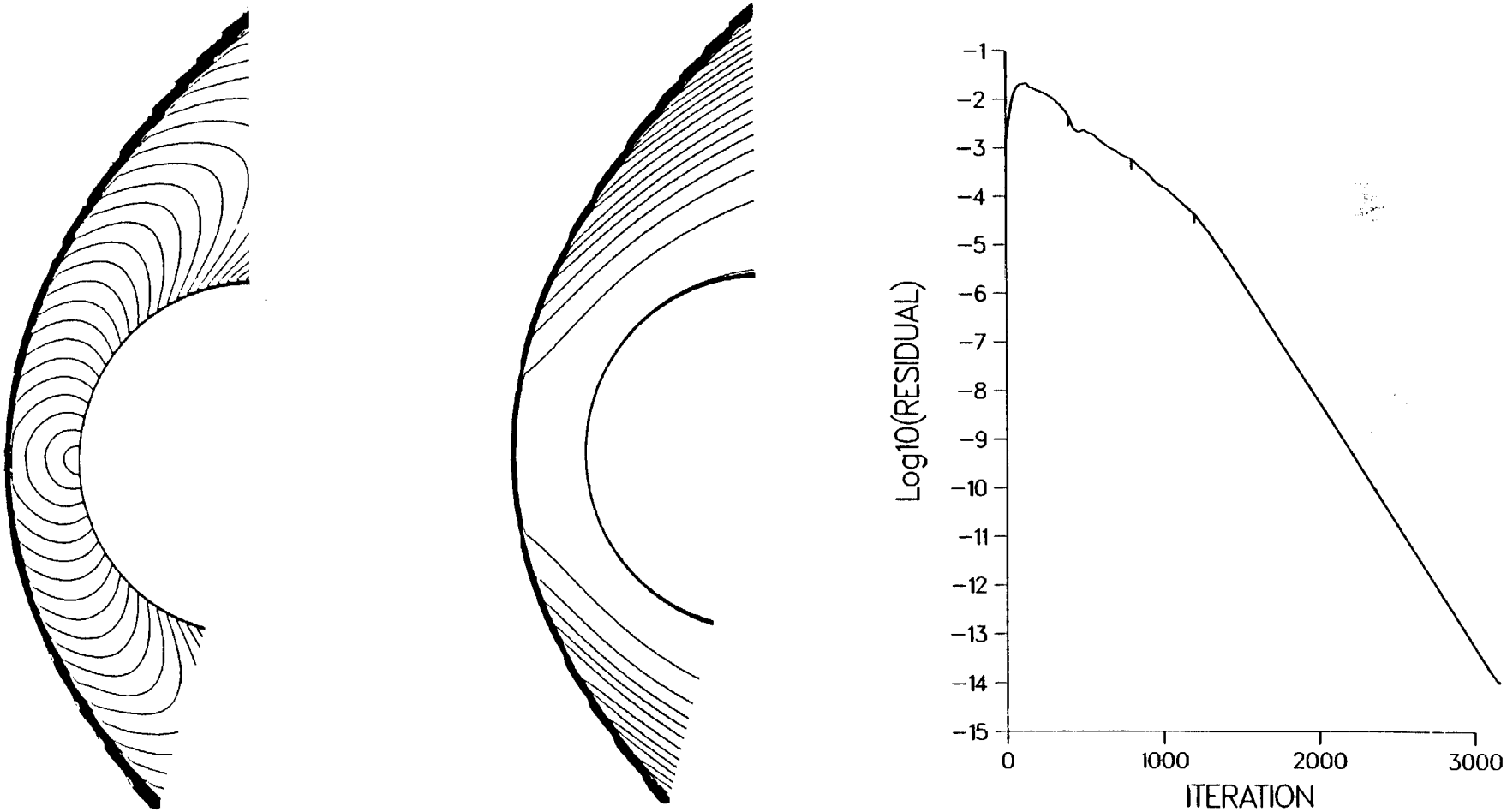

Fig. 8 Mach contours, entropy contours, and residual history for the steady viscous blunt body flow computed by algorithm (12) ($\theta = 1$, $\omega = 1/2$, full matrix form) with $M_\infty = 8.03$, $Re_D = 387,750$, $\gamma = 1.4$, and laminar flow.

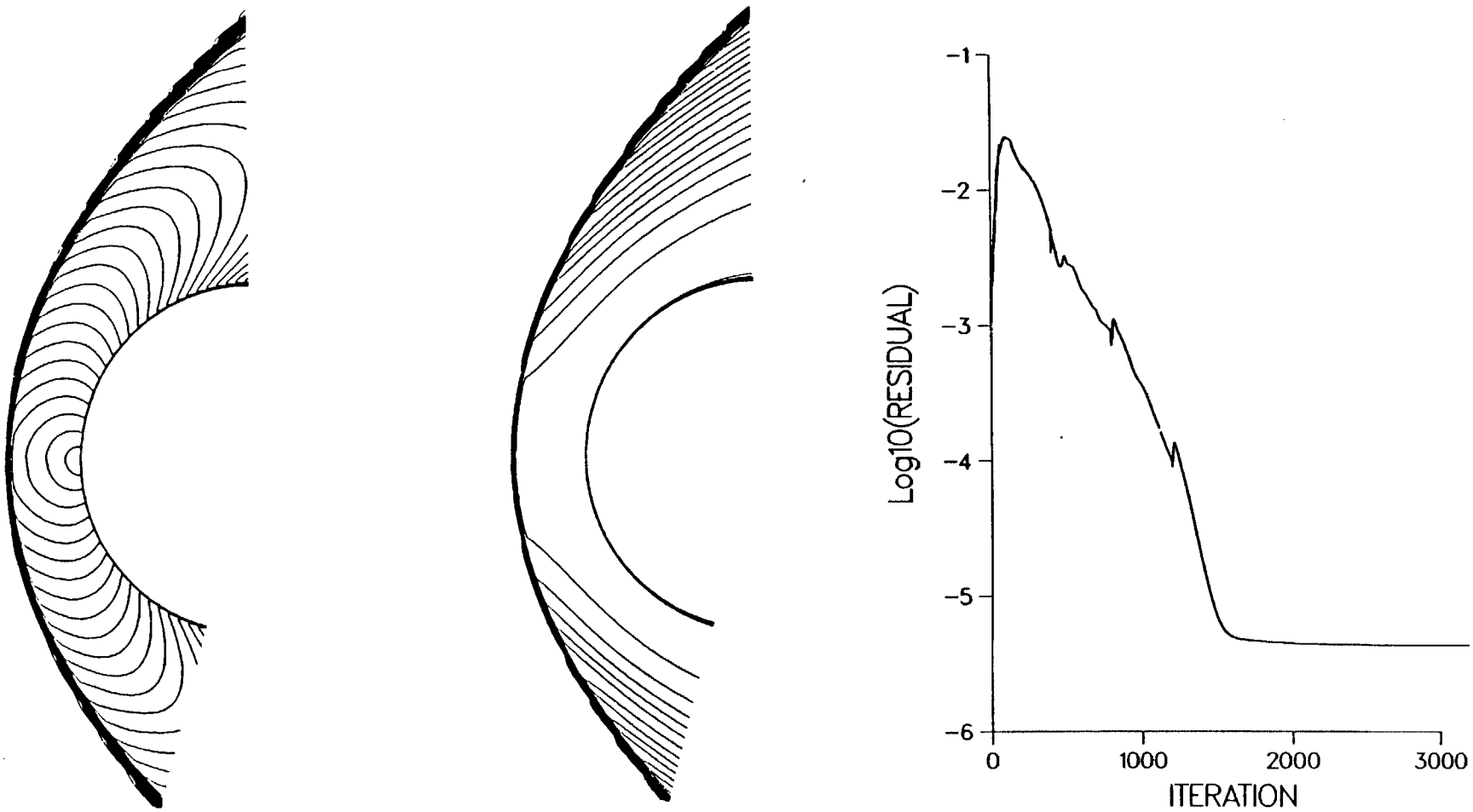

Fig. 9 Mach contours, entropy contours, and residual history for the steady viscous blunt body flow computed by algorithm (12,13) ($\theta = 1$, $\omega = 1/2$, diagonal form) with $M_\infty = 8.03$, $Re_D = 387,750$, $\gamma = 1.4$, and laminar flow.

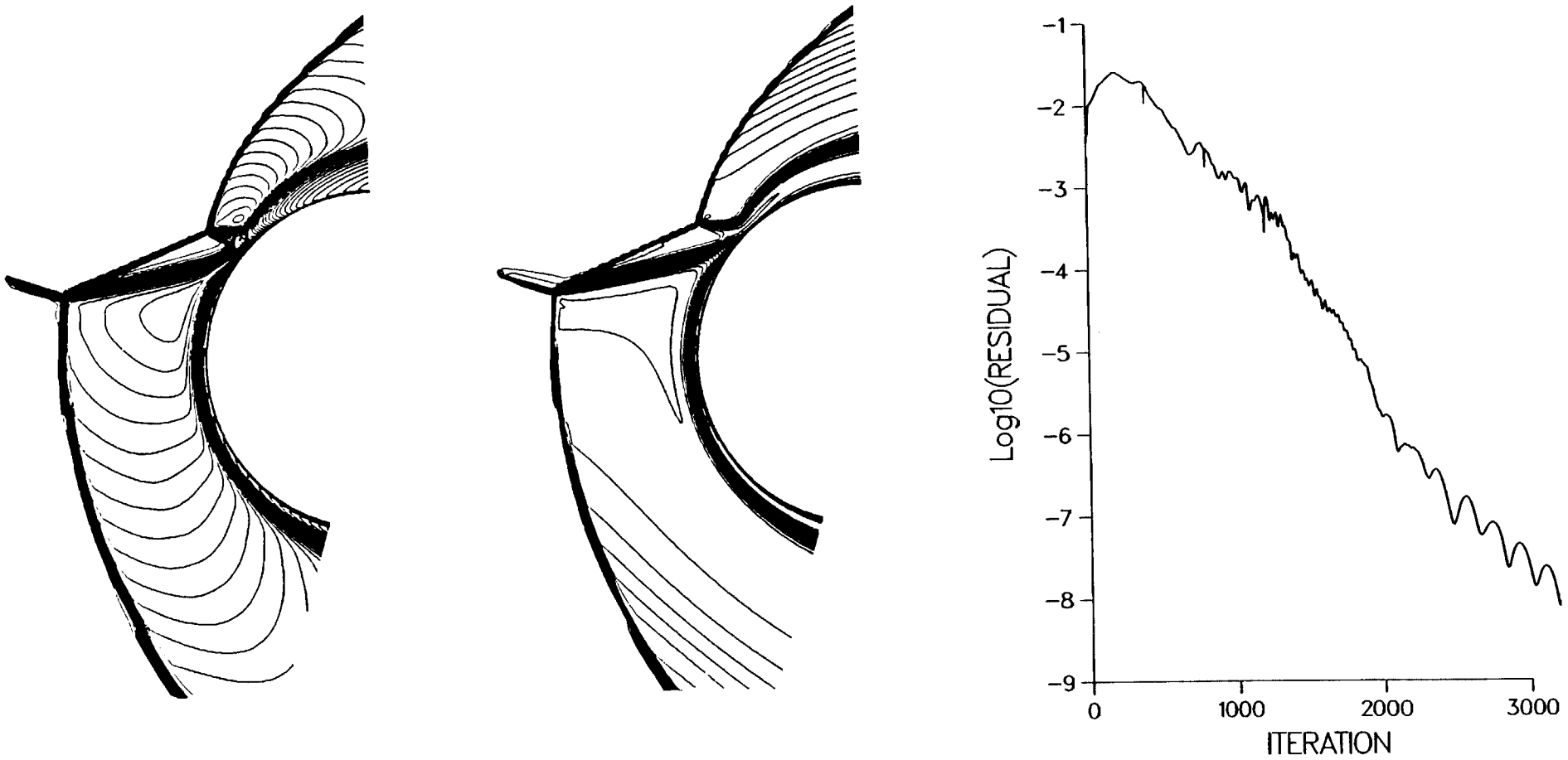

Fig. 10 Mach contours, entropy contours, and residual history for the steady viscous Type III shock interfernce flow computed by algorithm (12) ($\theta = 1$, $\omega = 1/2$, full matrix form) with $M_\infty = 8.03$, $Re_D = 387,750$, $\gamma = 1.4$, and laminar flow.

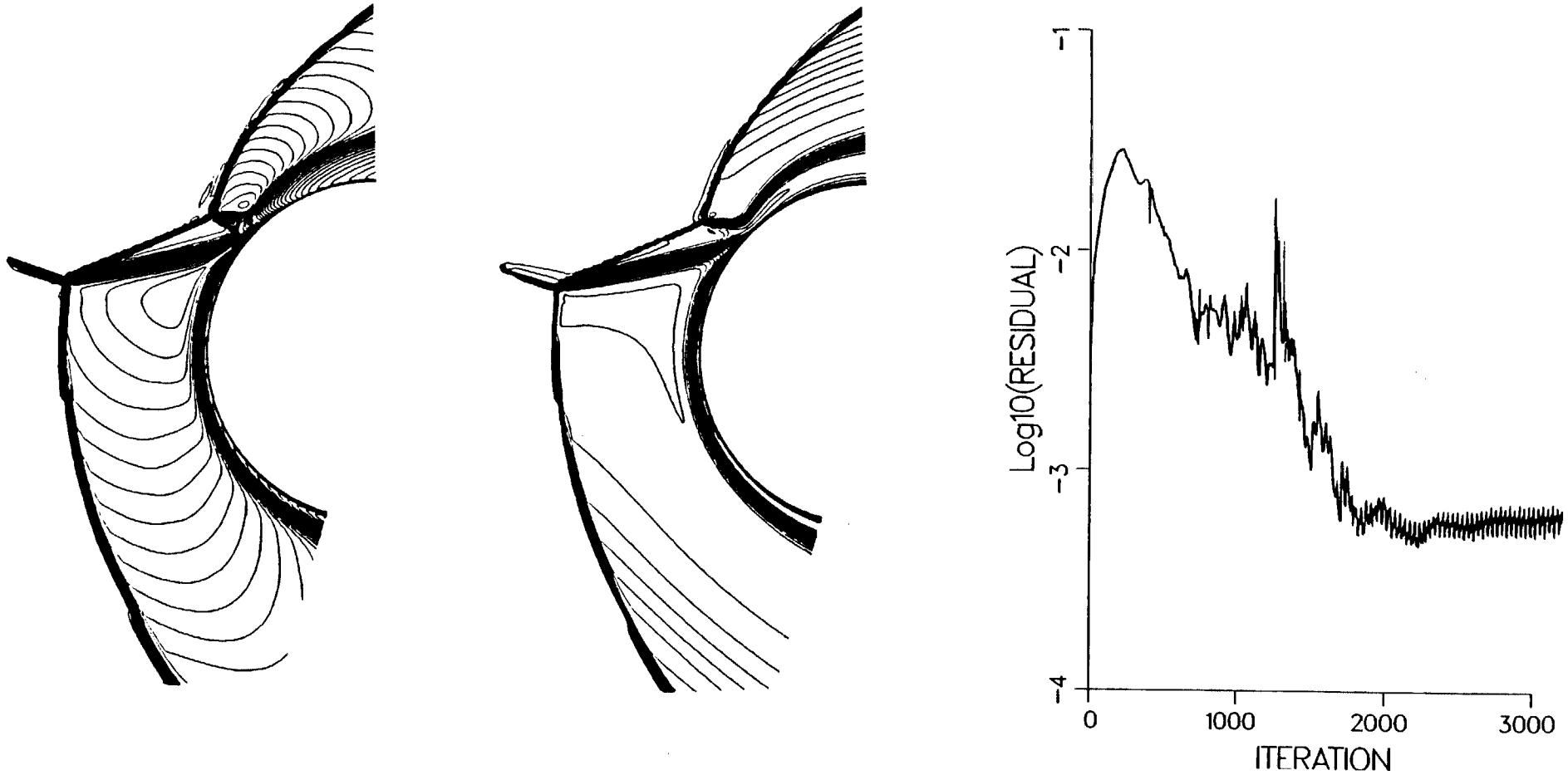

Fig. 11 Mach contours, entropy contours, and residual history for the steady viscous Type III shock interfernce flow computed by algorithm (12,13) ($\theta = 1$, $\omega = 1/2$, diagonal form) with $M_\infty = 8.03$, $Re_D = 387,750$, $\gamma = 1.4$, and laminar flow.

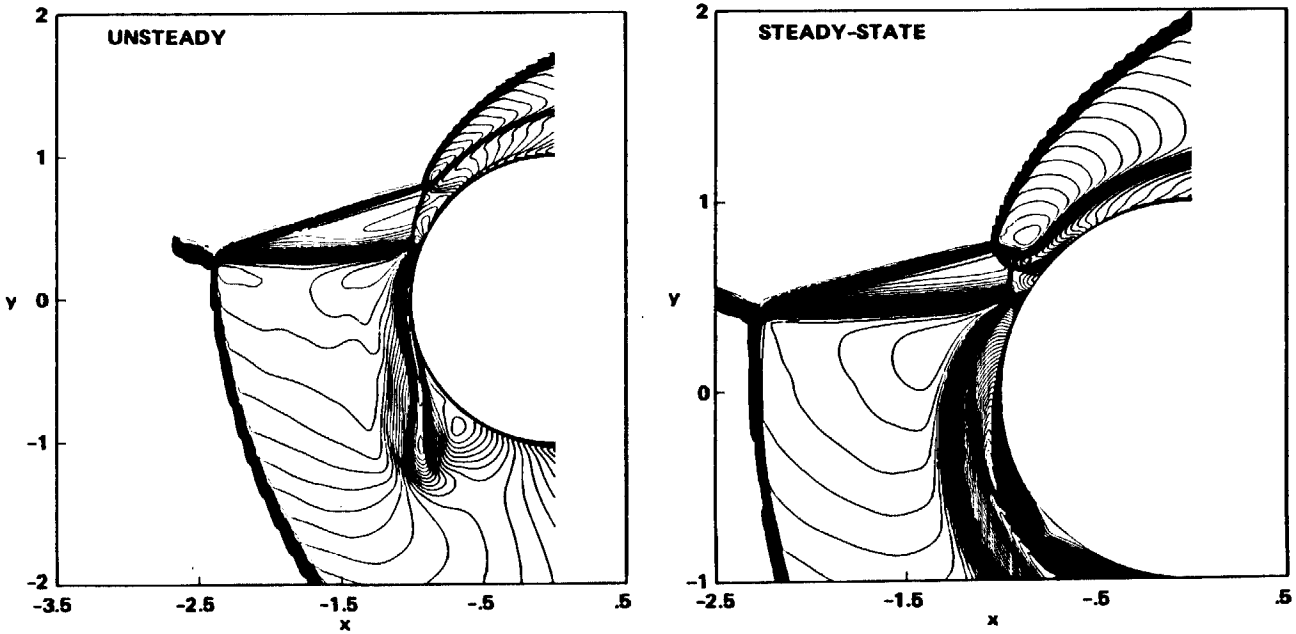

Fig. 12 The Mach contours of a two-dimensional viscous steady and unsteady hypersonic perfect gas computation by algorithm (12) ($\theta = 1$, $\omega = 1/2$, full matrix form) with $M_\infty = 15$ and $Re_D = 186{,}000$.

NASA National Aeronautics and Space Administration

Report Documentation Page

1. Report No.	2. Government Accession No.	3. Recipient's Catalog No.
NASA TM-100097		

4. Title and Subtitle

High-Resolution Shock-Capturing Schemes for Inviscid and Viscous Hypersonic Flows

5. Report Date

April 1988

6. Performing Organization Code

7. Author(s)

H. C. Yee, G. H. Klopfer, and J.-L. Montagné

8. Performing Organization Report No.

A-88148

10. Work Unit No.

505-60

9. Performing Organization Name and Address

Ames Research Center
Moffett Field, CA 94035

11. Contract or Grant No.

13. Type of Report and Period Covered

Technical Memorandum

12. Sponsoring Agency Name and Address

National Aeronautics and Space Administration
Washington, DC 20546-0001

14. Sponsoring Agency Code

15. Supplementary Notes

Point of Contact: Helen C. Yee, Ames Research Center, MS 202A-1, Moffett Field, CA 94035
(415) 694-4769 or FTS 464-4769

16. Abstract

A class of implicit Total Variation Diminishing (TVD) type algorithms suitable for transonic and supersonic multidimensional Euler and Navier-Stokes equations has been extended to hypersonic computations. The improved conservative shock-capturing schemes are spatially second- and third-order, and are fully implicit. They can be first- or second-order accurate in time and are suitable for either steady or unsteady calculations. Enhancement of stability and convergence rate for hypersonic flows is discussed. With the proper choice of the temporal discretization and suitable implicit linearization, these schemes are fairly efficient and accurate for very complex two-dimensional hypersonic inviscid and viscous shock interactions. This study is complimented by a variety of steady and unsteady viscous and inviscid hypersonic blunt-body flow computations. Due to the inherent stiffness of viscous flow problems, numerical experiments indicated that the convergence rate is in general slower for viscous flows than for inviscid steady flows.

17. Key Words (Suggested by Author(s))	18. Distribution Statement
Implicit shock-capturing methods Total variation diminishing schemes (TVD) Viscous hypersonic flows MUSCL, flux-vector splitting	Unclassified-Unlimited Subject Category – 64

19. Security Classif. (of this report)	20. Security Classif. (of this page)	21. No. of pages	22. Price
Unclassified	Unclassified	34	A02

NASA FORM 1626 OCT 86